Spring 2023

Tuned gold layer growth onto plasmonic sensing silver nanocubes via synthetic control of reduction potentials.

Nicolas Hall
Western Washington University, hallcoughdrop@gmail.com

Tuned gold layer growth onto plasmonic sensing silver nanocubes via synthetic control of reduction potentials.

By

Nicolas Hall

Accepted in partial completion of the requirements for the degree

Master of Science

ADVISORY COMMITTEE

Dr. Ying Bao, Chair

Dr. Manuel Montano

Dr. Steven Emory

WESTERN WASHINGTON UNIVERSITY

David L. Patrick, Dean

Master's Thesis

In presenting this thesis in partial fulfillment of the requirements for a master's degree at Western Washington University, I grant to Western Washington University the non-exclusive royalty-free right to archive, reproduce, distribute, and display the thesis in any and all forms, including electronic format, via any digital library mechanisms maintained by WWU.

I represent and warrant this is my original work and does not infringe or violate any rights of others. I warrant that I have obtained written permissions from the owner of any third party copyrighted material included in these files.

I acknowledge that I retain ownership rights to the copyright of this work, including but not limited to the right to use all or part of this work in future works, such as articles or books.

Library users are granted permission for individual, research and non-commercial reproduction of this work for educational purposes only. Any further digital posting of this document requires specific permission from the author.

Any copying or publication of this thesis for commercial purposes, or for financial gain, is not allowed without my written permission.

Nicolas G. Hall

June 6th, 2023

Tuned gold layer growth onto plasmonic sensing silver nanocubes via synthetic control of reduction potentials.

A Thesis
Presented to
The Faculty of
Western Washington University

In Partial Fulfillment
Of the Requirements for the Degree
Master of Science

by
Nicolas Hall
June 2023

Abstract

Metallic nanoparticles (mNPs) are commonly employed as sensors and detection tools due to their unique plasmonic properties. Silver NPs exhibit these properties in heightened capacity in comparison to other metals. However, Ag NPs are susceptible to oxidation, degradation over time and are biotoxic. These issues are commonly addressed by creating Ag-alloy NPs or by adding additional layers to Ag NPs. This work improves upon these methods by focusing on the growth of an Au layer onto Ag nanocubes (AgNCs), resulting in a layered Au-Ag NC (Au@AgNC). The resulting morphology of these Au@AgNCs are dependent on the synthetic pathway taken and can be difficult to control. This work focuses on understanding the Au@AgNC synthesis procedure and the reactions that drive the gold layer overgrowth. Primarily the galvanic replacement reactions (GRR) and its manipulation was studied. Reduction potentials and experimental parameters were investigated to better understand their role in the Au@AgNC synthesis. As specific pathways are encouraged or discouraged the resulting morphology can be readily controlled. The use of potassium iodide (KI) was studied as one route to manipulate the GRR dominance and role. This works provides detailed studies in the synthetic control of Au@AgNC morphology providing evidence for many common synthetic parameters used in the literature.

Acknowledgements

I would like to firstly thank Dr. Ruth Tinnacher for her support and help when deciding to go back to school. Without her support and advice, I would not have found Western Washington University.

I would like to thank the chemistry staff at Western Washington University involved in the teaching courses. Amy Cully, Meghan Blodgett-Carrillo, Britt Tyler, Dr. Raymond and Charles Wandler. You all made teaching for the first time a truly great experience and one of the most enjoyable parts of my time at Western. Special thank you to Dr. Michael Enright and Mark Lorenz for the patience and wiliness to learn with me, especially during my first quarter trying to figure out how to be a student again and relearning topics I had not seen in years. Dr. Michael Kraft for the more than generous time, effort, and support he has given me and the entire Bao research group. This lab depends greatly on your expertise and willingness to help us get the best possible results even if we push what is possible with the instrumentation.

I would like to thank the friends and amazing people I meet from the research group here at Western, Dr. Ying Bao, Anika Guo, Annabella Talbott, Ayomide Oluafemi, Griffin Cooper, Hosanna Abbay, Matthew Cossette, Meghan Burke, Nigel Ng, Oliver Vause, Racer Wagoner, Teagan Hamlett, Wynn Wee, Bailey Klinger, Joseph Almanza and Chloe Anderson. You each have made this experience worthwhile, and your support is the sole reason I finished this degree. Our discussions and time spent will forever be the most valuable part of this entire experience.

Lastly, I would also like to acknowledge Josh Basillio and the Seattle/Tacoma HxC community. You welcomed me in immediately and helped keep everything in perspective when research and school became overwhelming.

Table of Contents

List of Figures and Schemes

Chapter 1: Introduction

1.1 Metal Nanoparticles

Metal based nanoparticles (mNPs) serve as a tool for two of the most important techniques possessed by the scientific community; the detection and tracking of specific targets. These skills are required by nearly all industries and processes. Scientific and research communities rely heavily on detection and tracking to gain better understandings of our world and to improve the limits of what is possible. Metallic nanoparticles have become on the leading solutions to the challenges and goals of these various applications.

Metallic nanoparticles have grown in popularity in recent years and have become an expansive field of research with great interest, particularly because of their optical properties. Metallic NPs are particles composed of metals, commonly noble metals, such as Au, Ag, Pt, and Pd, that are on the nanometer scale, typically ranging from 20 nanometers to a few hundred nanometers. However, they can be on an even smaller scale such as quantum dots, which can be as small as 2-3 nm in diameter.[47] Noble metals are chosen for nanoparticle composition as non-noble metals often exhibit issues regarding stability, oxidization, and lack of distinct analytical properties [1].

Metallic nanoparticles have a wide range of properties that can be controlled and manipulated, allowing for almost endless variation. Controllable factors include size, shape, composition, solubility, functionalization, and morphology along with many others. Some of these attributes will be looked at in detail throughout this study. Even with the immense variety and forms that mNPs can possess, shared amongst many of them are unique optical properties.

1.2 Optical Properties

Many metallic nanoparticles display what is referred to as plasmonic properties. The electronic structure of the metals that compose these mNPs maintain free electrons which can result in the emission of electromagnetic flow and behavior. This flow creates an electromagnetic field called a plasmon. If these oscillations are manipulated by an excitation source, the resulting plasmons can create strong interactions with light, see **Figure 1.1.**[2] When the frequency of the resulting plasmon is less than that of the incident light, this electromagnetic field becomes heightened.[48] If the size of the particle has a resonance electronic frequency similar to or larger than the incident light, the material does not display increased surface plasmon resonance (SPR) properties.[2] This behavior is what makes the nanoscale uniquely useful.

The SPR peaks can be heightened even further based on the morphology of mNPs. Where corners and edges are present in mNPS, the plasmonic properties are stronger due to the higher exposed surface area of atoms and concentration of electromagnetic interactions. This is what is referred to as localized surface plasmonic resonance or LSPR.[50] These properties can be easily manipulated, influenced, and monitored via multiple methods of analysis and characterization.

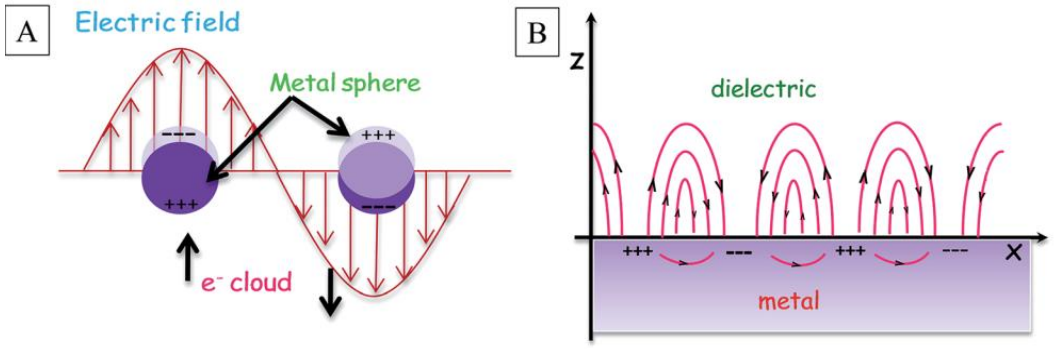

Figure 1.1. A) Electric field created by oscillation of nanoparticle electrons. **B)** resultant dielectric field.[7]

One of the significant benefits of plasmonic properties is that the resulting light scattering and absorption often occurs in the visible wavelength range. One example of when these visible interactions occur are as size and shape are manipulated. For example, silver nanocubes can be tuned to desired distinguishable colors ranging from vivid pink to turbid orange solutions simply based on size [3]. This important trial allows mNPs to be applied for general uses where simplified analysis can be done solely on color changes.[49] One example is the implementation of gold nanoparticles as sensors. A color change is observed when the gold nanoparticles interact with specific targeted chemical compounds, drugs or toxic substances.[37]

Ultraviolet-visible (UV-Vis) analysis is also commonly employed to analyze mNPs in a quantitative manner. The wavelengths absorbed and scattered by mNPs are typically within the UV-Vis range; approximately 100 nm to 900 nm. As mentioned previously, the optical properties of mNPs come in use as they possess SPR and LSPR interactions. These light interactions provide distinct peaks for UV-Vis analysis. **Figure 1.2 A** showcases an example UV-Vis spectra of gold nanorods.[6] These LSPR peaks can be fine-tuned to provide precise wavelengths. Dass et al., showed this tunability with silver coated gold nanorods by synthesizing nanorods with LSPR peaks spanning across a 450 nm range, ~ 400 nm to 850 nm.[4] Some studies have even managed to extend the wavelength range into the near-IR regions. For example, Chateau et al. achieved LSPR peaks up to 1850 nm with carefully designed gold based nano javelins.[5]

The LSPR properties can be tuned via the numerous parameters mentioned earlier. The combination of tuning several factors adds to the versatility of mNPs. Size and shape are two factors that can be relatively easily controlled to predictability shift the LSPR peak. The UV-Vis spectra shown in **Figure 1.2 A** provides an example of gold nanorods with a shifting LSPR as

the aspect ratio of the nanorod shape increases.[8] Control over the LSPR peak position allows for specificity when developing applications and implementation as sensing tools. An example of how composition controls LSPR peak position when the silver to gold ratio in spherical nanoparticles changes, **Figure 1.2 B**. Having such tunable control over the LSPR peaks is a huge advantage of mNPs allowing for usage across extremely varied applications.

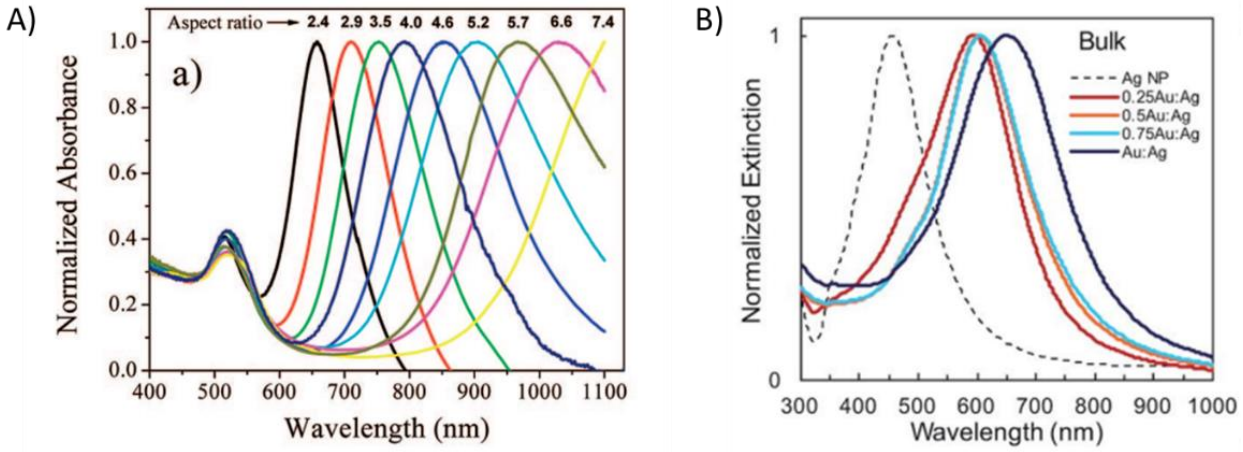

Figure 1.2. A) UV-Vis spectra of Au-Nanorods as the aspect ratio is increased, **B)** UV-Vis spectra of Au-Nanoparticles as the ratio of gold to silver is increased. [8,9]

The plasmonic properties of mNPs also go beyond simple UV-Vis analysis. Another common application of mNPs is Raman analysis. This method of analysis excites a sample of interest with incoming light and then monitors the light interactions as it is scattered inelastically. Raman is an excellent tool for the detection and tracing of target molecules. Systems can be easily studied by monitoring how light interactions change when mNPs are introduced with target species.[10]

Although interactions with light and Raman analysis can be performed with other materials, the use of mNPs results in enhanced interactions. This stronger interaction results in Surface Enhanced Raman Scattering or SERS. Typical Raman scattering occurs at significantly lower frequency than standard photon scattering; as infrequent as 1 in every 10^7 photons scattered.[10] Literature has shown that mNPs can enhance Raman detection significantly across a wide variety of nanoparticle forms. In **Figure 1.3**, amorphous-shaped gold nanoparticles are shown to enhance Raman performance both when free in solution and when immobilized on a substrate.[11,12] This enhanced signal was proven across a wide range of target molecules as well, displaying the wide reach of possible applications. Increasing the sensitivity of these detection methods and analysis techniques allows for significant advancements for both science and industry applications.

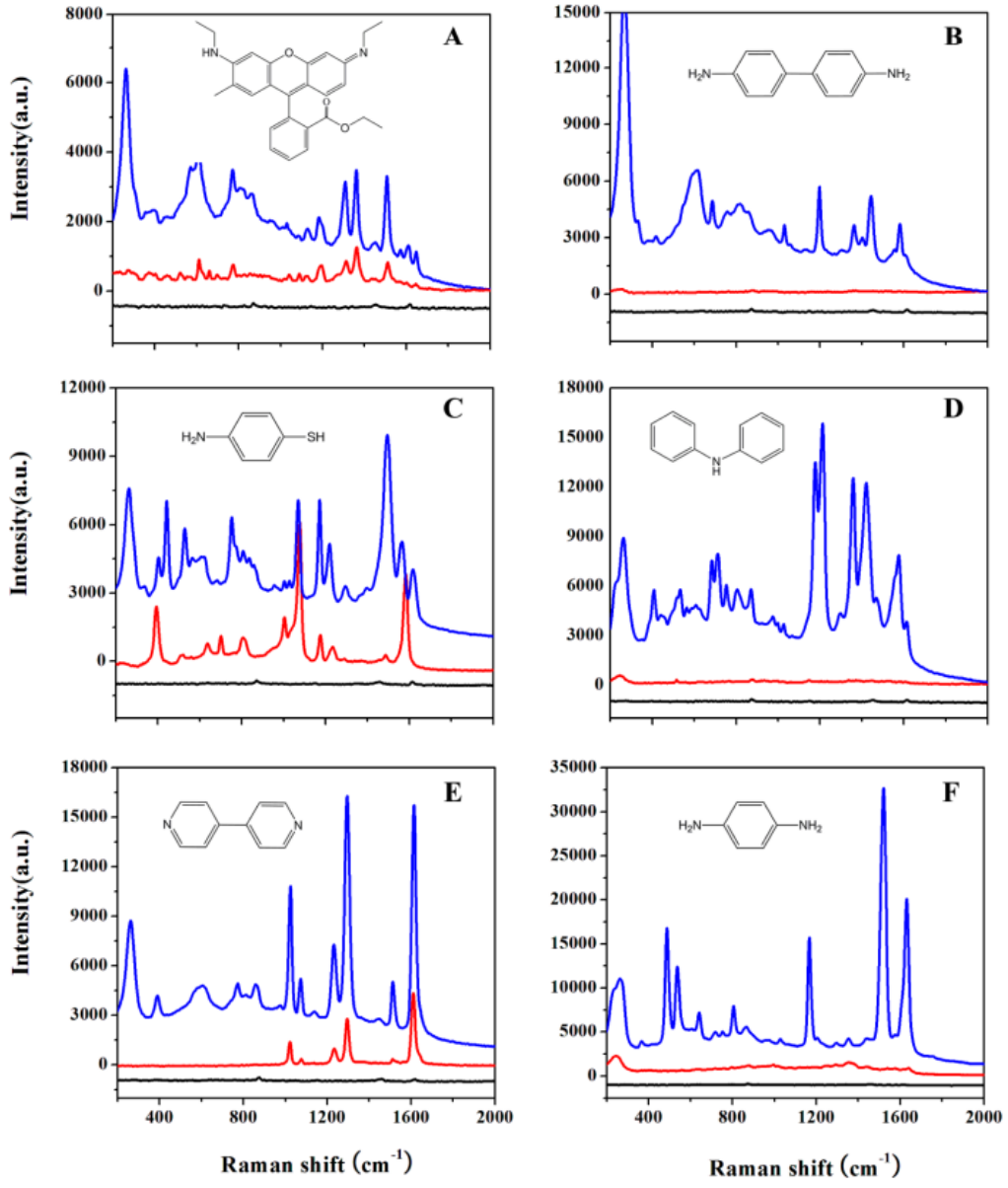

Figure 1.3: Blue line represents MIL with AuNP attached, red line represents MIL with AuNP in solution, black line represents MIP without AuNP. Rhodamine 6G (A), benzidine (B), 4-aminothiophenol (C), diphenylamine (D), 4,4-bipyridine (E), and p-phenylenediamine (F).[12]

Another physical trait of mNPs that has not been discussed yet is what is referred to as hotspots. The increased LSPR along the corners and edges mentioned earlier are commonly referred to as hotspots. Hotspots also result from near field coupling as nanoparticles form junctions with each other.[13] As the number of metal atoms increase in proximity to one another, the electromagnetic field becomes more intense with the increased oscillations. **Figure 1.4 A** shows this as the LSPR activity observed at the tips of silver nanotriangles is higher than along the edges.[16]

Numerous studies have been done on this concept and it has been reported that hotspots can increase SERS sensitivity by 10^9 fold or more.[14] Literature has found that in some situations, these hotspots are responsible for 85% of the recorded Raman signal even though they only account for approximately 6% of the surface area probed.[15] In similar fashion to the LSPR peaks, the hotspot activity can be tuned via mNP shape, size, and morphology. A study comparing silver nanotriangles to silver nanospheres via computational simulations of electric field distributions concluded that silver nanotriangles displayed more than 2 times the intensity on the corners than the spheres, **Figure 1.4 A.**[16]

The structures of mNPs can be tuned even further than just overall shape and geometry. Porous, fully hollow, or layered structures are often synthesized and as a result the optical properties will change. Li, et al showed that nanoparticles with a porous structure had more sensitive Raman detection when arranged in a manner to promote near field coupling hotspots.[17] This held true even as the porous structure had an additional layer of gold growth. **Figure 1.4 B** shows the resulting Raman spectra without any nanoparticles, with a solid silver nanoparticle array and with a porous gold/silver nanoparticle array.[17] **Figure 1.4 C and D** show scanning electron microscope (SEM) images of the solid and porous arrays respectively.[17]

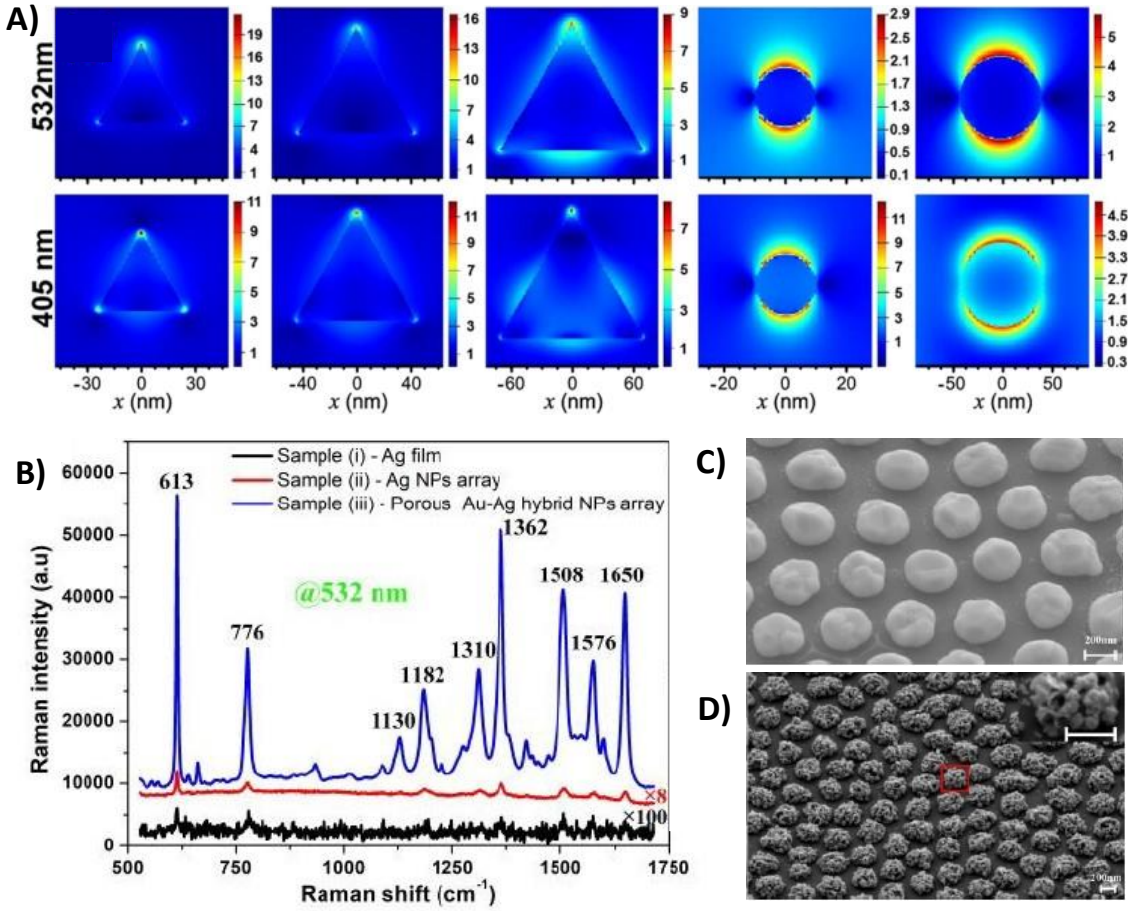

Figure 1.4. A) Electric field distributions of various NPs under varying excitation wavelengths[16] , **B)** Raman spectra at 532 nm excitation of Ag and Au-Ag hybrid NPs [17], **C)** SEM of the Ag NPs array, **D)** SEM of the porous Au-Ag hybrid array.[17]

These various morphologies are relevant as this study will focus on silver nanocubes (AgNCs) and their subsequent manipulation into gold coated silver nanocubes (Au@AgNCs). The benefits of both AgNCs and Au@AgNCs will be discussed in the next sections as well as their drawbacks and the current literature understanding of these particles.

1.3 Silver Nanocubes

Silver nanocubes are of particular interest for several reasons, stemming from both their shape and composition. The cubic formation provides benefits as it maintains sharp corners, creating the SERS hot spots mentioned previously. In a comparison study of electronic field intensity distributions via simulations, silver nanocubes outperformed with a max value of 17 volts per meter (V/m) while silver nanorods and nanospheres only had max intensities of 5 V/m and 1.5 V/m respectively.[18]

One reason why silver is viewed as a preferred noble metal for mNPs is due to its distinct LSPR peak. Palladium and copper based nanocubes both have LSPR peaks that can become quite broad and span approximately 100 nm.[19,20] Silver nanocubes, on the other hand, have sharp distinct peaks that that can span less than 10 nm.[21] Maintaining narrow LSPR peaks is a huge benefit as it allows for easier analysis and more versatility. As mNPs are functionalized the LSPR peak sharpness is often lost. Starting with a sharper peak allows for easier distinction as these mNPs are functionalized.

Gold is often chosen as the overgrowth material for a variety of reasons. Gold is a more expensive noble metal, making it more economical for gold to serve as a thinner outer layer rather than the bulk material. Synthetic techniques using gold as the bulk material have also shown difficulty in creating reliable materials with high yields.[22] Silver and gold also share similar properties, allowing them to work in tandem easier than other noble metals. The physical and crystal structure of gold and silver share the same unit cell structure of face centered cubic, as well as similar lattice constants resulting in an ideal metal pairing.[34]

Despite its strong plasmonic activity, AgNCs have a few associated drawbacks. One significant drawback of AgNCs is that silver is toxic to biological systems. This is extremely

limiting to which applications silver nanoparticles may be candidates for. Atrophy in mammalian life as well inhibition of photosynthesis in plants have been observed due to silver nanoparticle interference.[23] This is a major setback for medical and biological applications and has driven forward efforts to minimize or eliminate the toxicity of mNPs. Some attempts to address this issue involve the sulfidation of the silver NPs, reducing the possibility of silver leaving the nanomaterial and entering its surrounding medium.[24] The typical synthesis used to create AgNPs commonly involves non biocompatible and harsh chemicals, such as sodium borohydride or hydrazine.[25] There has been progress in developing more biologically favorable syntheses, such as the use of glucose as a reducing agent rather than sodium borohydride.[25]

Silver is also prone to oxidation which raises a couple of concerns. As AgNCs oxidize, their stability decreases and the cubic shape is lost. This results in non-distinct shapes that no longer possess the ideal LSPR peaks or SERS hotspots. Some studies have even shown that this shape loss can occur in under two minutes under certain conditions.[27] The release of silver from this loss of shape is also a concern for the biotoxicity mentioned previously. Another drawback of AgNCs is the LSPR peak range, which is generally limited to the range of approximately 450 nm to 900 nm.[28] This prohibits its usefulness for some systems where smaller or longer wavelengths are required.

Some studies have found ways to address multiple of these downsides with singular solutions. One method is to use a secondary metal to coat the AgNPs or to create an alloy layer. These alloy layers have been shown to effectively reduce harmful biological effects of AgNPs while also improving stability.[26] This additional metallic layer adds increased versatility and use of AgNCs. The study presented here will focus on the process of creating an ‘overgrowth’ of an additional metallic layer on AgNCs.

This overgrowth can help improve stability and reduce the oxidation of the silver while still maintaining the desired plasmonic properties. However, Au@AgNCs have a few drawbacks that stem from the mechanism and overgrowth process of the original AgNCs. These drawbacks and the Au@AgNC overgrowth will be discussed in detail in the next section.

1.4 Overgrowth

This section will focus on the overgrowth process as it is the primary question and intent of this work. **Chapter 2** will discuss the experimental details and set up of this project in greater detail.

The process of overgrowth occurs as a separate synthetic step using pre-synthesized AgNCs. In brief, to synthesis AgNCs, a gold seed, 2-3 nm, is synthesized and then used as a nucleation site to create a larger gold "core", approximately 11 nm.[29,30] By carefully choosing surfactants, reducing agent, and capping agents, a cubic structure is obtained by depositing silver onto gold 'cores' resulting in a single gold core surrounded by silver. The cubic structure is a result of preferential growth along selected facets that are orchestrated by the surfactants used. **Chapter 2** will go into further detail. In the standard synthetic procedure, the resulting AgNCs have an edge length of approximately 40 nm.[31] When completing a gold overgrowth, the resulting size of the Au@AgNCs increases depending on various reaction conditions, such as the amount of Au introduced into the system. When using typical literature-based procedures, NC size is increased

by approximately 30 nm as the Au overgrowth occurs. **Scheme 1.1** shows a brief overview of this process.[32]

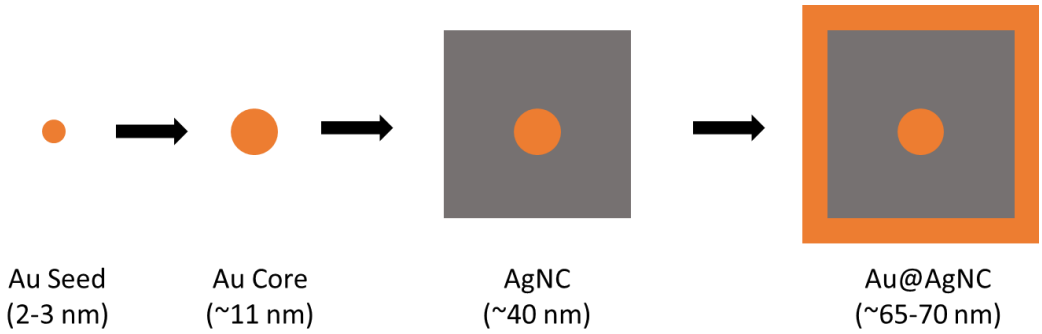

Scheme 1.1. Overview of the synthetic pathway taken to create Au@AgNCs.

To create Au@AgNCs, gold typically starts out as a salt compound such as chloroauric acid, $HAuCl_4$, where gold is in the Au (III) oxidation state. A reduction agent is introduced to reduce the Au (III) into Au (0), which then creates a system that favors deposition onto the AgNC. Since reduction of the Au is required, it might seem more logical to use a gold precursor with a different oxidation state such as Au (I) to minimize the reduction required. However, Au (III) minimizes some issues that arise with using the lower oxidation state precursors.

One reason for using gold in its Au (III) state is that the gold will oxidize slightly slower than the Au (I) state. Literature has reported when Au (I) is used as the starting material it oxidizes at fast enough rate that procedures become difficult to control and repeat reliably.[33] Another issue arises when later functionalization or manipulation is needed, as leftover Au (I) can easily facilitate metal ion quenching, requiring even more procedural steps and complications.[33]

In an ideal scenario after Au (III) is reduced to Au (0), it would deposit directly onto the AgNCs without any changes to the original AgNC structure, as shown in **scheme 1.1**. However, this is not commonly observed. Instead of the ideal deposition, galvanic replacement reactions (GRR) take place in tandem.

Galvanic reduction reaction occurs as a result of the reduction potentials in the system. As $HAuCl_4$ is introduced and the gold is reduced, chloride ions become available, which then interact with Ag. This creates a scenario that will prefer the formation of AgCl over Ag (0) in the bulk nanocube. Looking at **scheme 1.2 (2) and (3)** we can see that the reduction of Au (III) is favorable as it has a positive potential compared to the standard hydrogen electrode (SHE). This reaction along with the half-cell potentials are shown in **scheme 1.2.**[28]

(1) $3Ag_{(s)} + AuCl_4^-{}_{(aq)} \rightarrow Au_{(s)} + 3AgCl_{(aq)} + Cl^-{}_{(aq)}$

Half Cell Reactions		E_0
(2)	$AuCl_4^-{}_{(aq)} + 3e^- \rightarrow Au_{(s)} + 4Cl^-{}_{(aq)}$	1.00
(3)	$AgCl_{(aq)} + e^- \rightarrow Ag_{(s)} + Cl^-{}_{(aq)}$	0.223

Scheme 1.2. 1) reaction of silver nanocubes with chloroauric acid, **2-3)** half-cell reactions and reduction potentials of $AuCl_4^-$ and AgCl.[28]

Looking at **Scheme 1.2 (2) and (3)**, the reduction potential of AgCl/Ag is far lower than that of $AuCl_4^-$/Au, meaning that the reduction of Au and its deposition will dominate the system. This results in the GRR and Ag leaving the bulk nanocube as it oxidizes, forming AgCl salt compounds.

Due to the stoichiometry of the system, for each gold atom reduced, three chloride ions become available allowing for three silver atoms to leave the bulk nanocube. This results in voids as the gold does not replace the silver at the same rate. This is referred to the etching of the AgNCs. To further this complication, when the silver leaves the nanocube structure, it does so in

a manner that expands the initial voids or etching rather than dissipating from new sites.[34] Often this results in completely hollow structures without any bulk silver remaining, see **Scheme 1.3**. This is significantly different than the ideal structure seen in **Scheme 1.1**. Structures created from the GRR, can create non-ideal situations as the plasmonic properties of silver are preferred over gold.

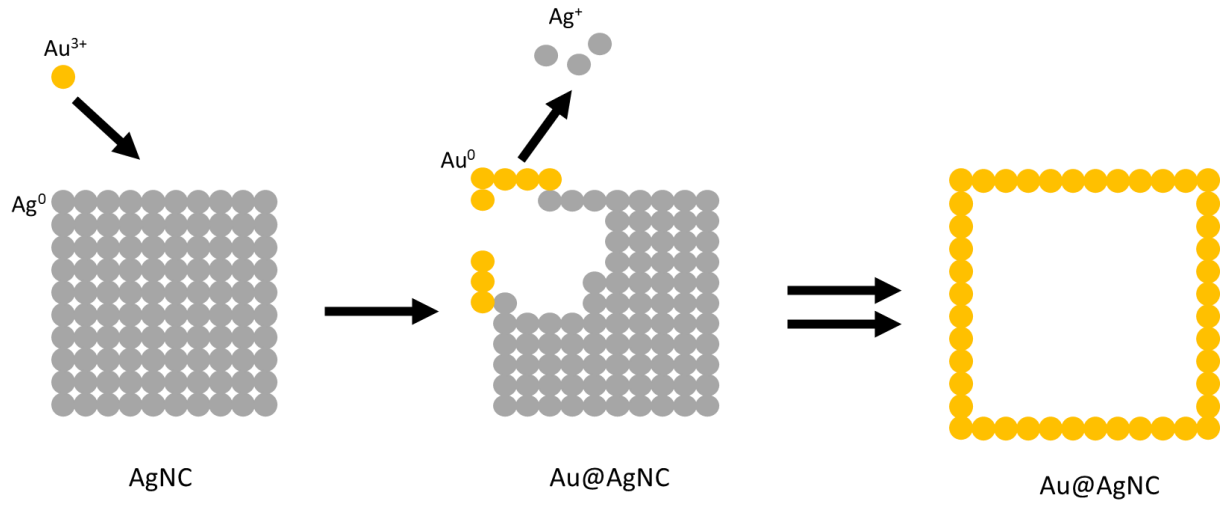

Scheme 1.3. Overview of the galvanic replacement reaction to form hollow Au@AgNCs.

To deposit a layer of gold in a controlled manner, the process can be manipulated to be driven by preferred potentials. Reduction potentials can be controlled with varying predictability, allowing the possibility of synthetic control over the nanocubes' final morphology. This work aims to manipulate these reduction potentials to gain full synthetic control of these reactions.

Some studies regarding this reduction potential manipulation have been done such as Mayer et al. and Sneed et al.[32,35] However, most literature takes an approach to AgNC synthesis that uses surfactants and reducing agents such as ethylene glycol (EG) or poly(vinyl pyrrolidone) (PVP) which require high temperatures in more controlled continuous titration scenarios.[36] Temperatures of 150 ^{0}C or higher are required if this route is taken and typically requires time sensitive quenching.[36] While this is easily achievable in most laboratories, it adds excess sources

of human error and increases the difficulty and concerns for large scale applications. This leads to the need for further studies using other growth methods such as the one presented in this work. Rather than the multistep titrations using EG and PVP, this work will focus on the simplified synthetic procedure involving cetrimonium chloride as a surfactant material to create the AgNC that will then be used to create Au@AgNCs.

1.5 Goal of project

The work presented here aims to study gold overgrowth onto silver nanocubes as reduction potentials are manipulated by the inclusion of potassium iodide in the system. This will be accomplished by a series of laboratory experiments followed by characterization and analysis. Conducting the full synthetic steps and process will also allow for the study of experimental conditions not often studied in nanoparticle research. The following chapters will present a detailed synthetic procedure, analytical and characterization techniques, and finally a results and discussion of the overgrowth studies conducted along with conclusions and the related challenges observed.

Chapter 2: Materials and Methods

2.1 Chemicals, Equipment, and Instrumentation

Silver nitrate ($AgNO_3$) was purchased from Alfa Aesar. Sodium borohydride ($NaBH_4$), hexadecyltrimethylammonium chloride (CTAC), hydrogen peroxide (H_2O_2), and sodium hydroxide (NaOH) were all purchased from Sigma Aldrich. L-ascorbic acid (L-AA) and sulfuric acid (H_2SO_4) were both purchased from Fisher Scientific (USA). Hexadecyltrimethylammonium bromide (CTAB) was purchased from Acros Organics. Potassium iodide (KI) was purchased from Thermo-Scientific. Sodium chloride (NaCl) and nitric acid (HNO_3) were purchased from Macron Fine Chemicals. Gold (III) chloride trihydrate ($HAuCl_4 \cdot 3H_2O$) was purchased from Honeywell Fluka. Hydrochloric acid (HCl) was purchased from VWR. All chemicals were as received from the manufacture and used without further purification.

All glassware used was precleaned with Aqua Regia, a cleaning solution consisting of a 1:3 ratio of nitric acid and hydrochloric acid to remove any trace metals or contaminates. After an aqua regia wash all glassware was rinsed in excess water and then then dried at 110 ^{o}C. All water used in this work was obtained from a Direct-Q 3UV with a Milli-Q grade of 18.2 MΩ and total organic carbon less than 10 ppb and is referred to as nano pure water (NPW). Controlled additions via syringe pumps used two different pumps, Golander L-AA-02 and Cole-Parmer 75900-50, using 10 mL sterile syringes and 3.175mm x 6.35 mm NP-PVC tubing.

For all centrifugation an Eppendorf S425R was used at ambient temperature. An Agilent Cary 3500 double beam UV-Vis spectrometer with a Xe flash bulb and a multicell Peltier holder with heating and stirring capabilities was used for all UV-Vis analysis.

Scanning transmission electron miscopy images were collected used a JEOL JSM-7200F with secondary electron, back scatter electrons and STEM detectors with an auxiliary Oxford EDS system for energy dispersive x-ray spectroscopy (EDS) analysis.

2.2 Gold Seed Synthesis

The standard procedure for gold seed was adopted from Ma et al. (2010) with minimal modification and is described below.[30]

Firstly, 45 mL of NPW was chilled using an ice bath for later preparation of a $NaBH_4$ solution. Using a 20 mL scintillation vial, a solution of 100 mM CTAB and 0.25 mM $HAuCl_4$ with a final volume of 10 mL was prepared and mixed by inversion. CTAB is used to stabilize the nanoparticles and avoid agglomeration as they begin to form clusters and nucleation sites.[39]

Next using the chilled NPW a 10 mM $NaBH_4$ solution was prepared. It is important that the $NaBH_4$ solution is prepared quickly, and that chilled water is used in to slow the reaction of $NaBH_4$. If this is not done complete reduction will not occur, and the number of nucleation site will be less resulting in larger than desired seeds. As the $NaBH_4$ solution is mixed by inversion slight pressure builds up that needs to be released. Immediately after preparation, 0.3 mL of the 10 mM $NaBH_4$ solution was pipetted into the prepared solution of $HAuCl_4$ and CTAB.

The $NaBH_4$ reacts quickly reducing the gold salt allowing for the formation of nanoclusters that will serve as nucleation and growth sites as the reaction proceeds.[39] The solution is inverted to mix and immediately stored away from light for a 3-hour period. The solution becomes a tea brown color instantly. This indicates the gold precursor salt is being reduced and nanocrystals are forming. If the color change does not appear within the first few seconds, then the solution needs to be remade. The solution may turn slightly pink-white over the

3-hour period. This pink-white color change is due to the CTAB falling out of solution. If this occurs the CTAB is redispersed by placing the solution briefly in a heated water bath at 45 ^{o} C until no crystals remain. **Figure 2.1 A** provides an example of the Au seed; **Figure 2.1 C** provides an example of the Au seed after CTAB has fallen out of solution.

Purification is not required at the end of the 3-hour period and the gold seed is used as is. The gold seed solution only remains useable for one to two days. After that a fresh seed solution should be prepared. The color of the Au seed solution will become browner as it ages and loses stability. After the gold seed has been synthesized, it was then used to create a gold core solution as described in the next section.

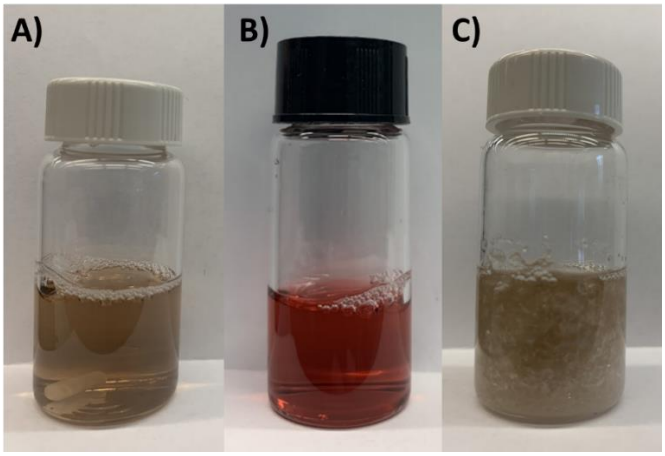

Figure 2.1. Image of **A**) gold seed, **B**) gold core, and **C**) gold core after CTAB has fallen out of solution.

2.3 Gold Core Synthesis

The standard procedure for gold seed was adopted from Ma et al. (2010) with minimal modification and is described below. [30]

Using a 20 mL scintillation vial a growth solution was prepared containing 6 mL of 0.5 mM $HAuCl_4$, 6 mL of 200 mM CTAC and 4.5 mL of 100 mM L-AA. This solution is mixed via stir plate with gentle stirring, 200 rpm, and is kept from direct light by foil. Once the growth solution was sufficiently mixed, 0.3 mL of the synthesized gold seed from **section 2.2** was added to the solution. The growth solution was then left at room temperature for 1 hour while stirring at 500 rpm. This solution will turn a dark red-purple color immediately after addition.

After the core growth solution stirred for an hour, the solution was purified via centrifugation, described below. This solution should be purified soon after the hour reaction period. If the solution is left to sit longer the size of the cores will vary compromising future synthesis parameters. The purification process requires multiple steps to ensure that all the gold cores are collected.

First the bulk solution was centrifuged at 14,500 rpm for 30 minutes. The supernatant was then collected and centrifuged again at the same settings. The pellet is redispersed with NPW to the original volume. After the initial supernatant is centrifuged, the new supernatant is collected once more and centrifuged again at the same settings. The second pellet is then redispersed using the redispersed solution from the initial pellet. Once the third centrifugation cycle has finished the supernatant should be clear to very faintly colored. This supernatant can then be discarded, and the third pellet can be redispersed using the solution that contains the first two pellets. If the solution is still strongly colored after the third round of centrifugation more rounds of centrifugation are required. It is crucial that this step is repeated consistently, and all the core is collected as this will affect the core concentration that will then be used for all cube synthesis. If this is properly done as described the core size should be approximately 11-15 nm.[30]

Figure 2.1 B provides an example of the as described purified Au core. **Figure 2.2 A and B** provide examples of STEM images and average size plot of the as described Au cores.

The purified gold core should be stored away from light at room temperature. This solution can be stable for multiple months and will turn a darker brown color once it is no longer stable. UV-Vis analysis should be collected using the procedure described in **section 2.5.1.** The UV-Vis spectrum of the Au core should have a broad peak at approximately 520 nm. Before each use a UV-Vis spectrum should be collected to ensure the seed is still within ~5 nm of the original scan. The UV-Vis spectra should be relied upon more than the color when determining the quality of the gold core. **Figure 2.2 C** provides an example UV-Vis spectrum of the as described Au core.

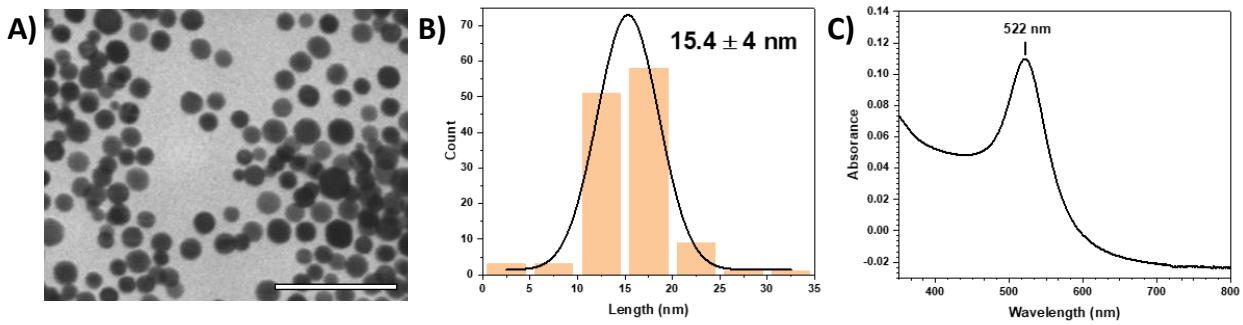

Figure 2.2. **A)** STEM image of gold cores, scale bar represents 100 nm, **B)** gaussian distribution of gold core size, average diameter 15.3 +/- 4 nm, **C)** UV-Vis spectrum of gold cores with a peak absorbance at 522 nm.

During core synthesis the surfactant is changed from CTAB to CTAC as way to control the growth of the core size. During seed synthesis CTAB is present to stabilize the particles and avoid agglomeration but at this stage a capping agent, CTAC, is required to control growth

direction and size. Although CTAB can also serve as a capping agent literature has found that CTAB leads to larger particles with lower uniformity in both size and shape.[30,39] A uniform gold core is important as it is one of the parameters that affects AgNC size. It is even common in nanoparticle literature to tune particle size and plasmon properties by controlling the core size, proving that this is an important parameter.[41, 42]

During the core synthesis L-AA is used as the reducing agent instead of $NaBH_4$. Seed synthesis requires a strong reducing agent such as $NaBH_4$ to fully reduce gold salt to the elemental state for nucleation sites occur.[40] After gold seeds have been obtained, a weaker reducing agent is used, such as L-AA, to prevent further nucleation sites from forming while ensuring that the gold salt precursor is still being reduced sufficiently. Literature has done significant studies on the reduction mechanisms of the L-AA and there is still some debate regarding its exact pathway, but it has been proven to successfully reduce Au (III) to Au (0).[45] The use of L-AA also has other benefits at this stage.

Literature has reported that the use of L-AA for nanoparticle synthesis results in sharper UV-Vis spectrums when compared to other reducing agents such as, sodium borohydride or hydrazine.[43] Ascorbic acid is also biocompatible and has even been used in bone tissue engineering, while stronger reducing agents such as hydrazine and sodium borohydride are not biocompatible.[44]

2.4 Silver Nanocubes Synthesis

Silver nanocube synthesis was adopted from Yang et al, (2017) procedure with minimal modification as described below.[38] This method is often referred to as seed-mediated growth as it starts with an initial Au seed.

To begin a solution was prepared in a 20 mL scintillation vial that contained 15 mL of 20.0 mM CTAC and 0.3 mL of the purified Au core described in **Section 2.2**. It is crucial that purified core is used. If the core solution is not purified excess CTAC and CTAB will interfere with the AgNC formation. This solution was then placed into an oil bath at 60^0 C for 30 minutes while capped. Both the oil bath and the solution were kept stirring at 500 rpm to maintain consistent heating.

During the heating period the required solution for the silver overgrowth was prepared. This was accomplished by first preparing a 100 mM solution of L-AA. A solution of 2.0 mM $AgNO_3$ was then prepared for dispensing using a syringe pump. It is important to have the syringe pump ready to dispense the $AgNO_3$ before the next step, additions in quick succession are required.

After the 30-minute heating period ended the cap was removed and 1 mL of the 100 mM L-AA solution was added by pipette while maintaining stirring and heat. As soon as the L-AA was added 2.4 mL of the $AgNO_3$ solution was added via syringe pump at a rate of 1 mL per min. Once the $AgNO_3$ addition was complete the vial was recapped and then left in the oil bath while stirring at $60\ ^0$ C for a minimum of 4 hours.

This solution should initially become a turbid yellow and then gradually shift to a turbid gold brown color during the reaction period. **Figure 2.3 A - C** provides examples of the as described AgNCs during various points of the synthesis. If this solution is pink in color, the L-AA was likely not added and there will be a high concentration of nanorod impurities.

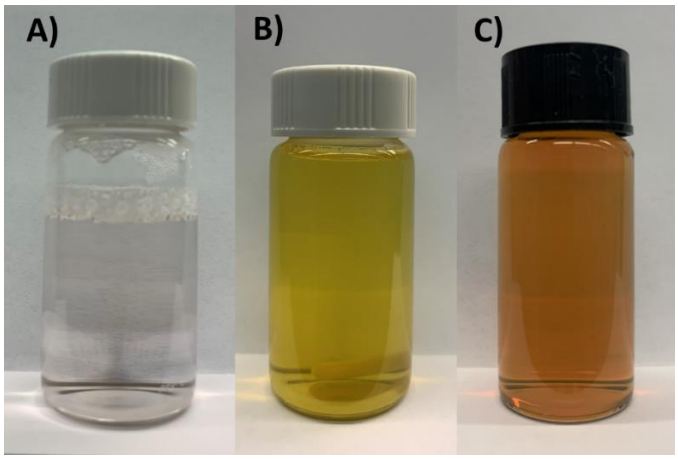

Figure 2.3. **A)** AgNC growth solution before silver addition, **B)** AgNC growth solution after silver addition, **C)** AgNC solution after reaction completion,

Once the reaction period is concluded, the solution is cooled to room temperature and then purified via centrifugation at 11,000 rpm for 15 minutes. The pellet is collected and redispersed to the original volume using NPW. The purified solution is then parafilmed and stored away from light.

UV-Vis analysis should be done using the procedure described in **Section 2.5.1** to determine the wavelength of the AgNCs. Silver nanocubes can have a wide range of plasmonic peaks based on their size, but generally range from 400 nm to 520 nm.[32, 31] Using the procedure described here the typical peak is 440 nm to 450 nm. Slight shoulder peaks may be present due to other plasmonic modes displayed by silver in the 350 nm to 450 nm range.[32] The average length of the AgNC produced from the as described synthesis range from 32.2 nm – 38.2 nm ± 2 nm. An example of the STEM images, average size plot and UV-Vis spectrum can be found in **Figure 2.4**. The average particle count in the AgNC solution is shown in **Table 3.2**. The AgNC solution is stable for long periods of times when stored at room temperature away from light and

parafilmed to reduce risk of oxidation. Before each use a UV-Vis spectrum was collected to ensure that the wavelength has not significantly shifted.

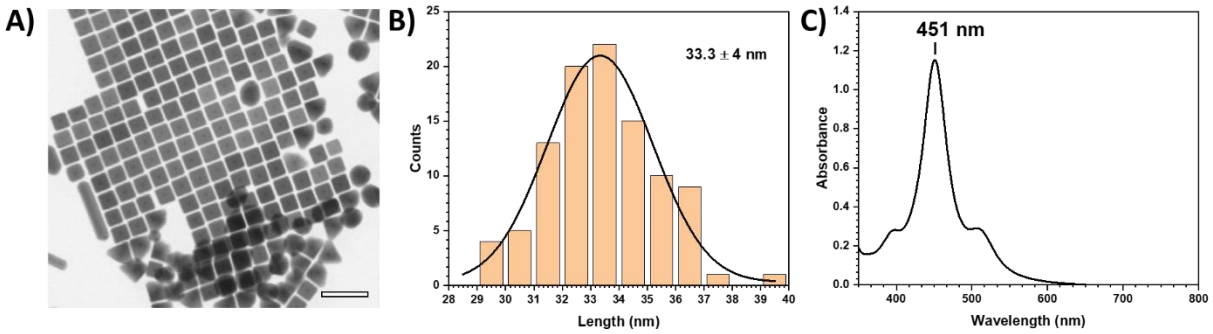

Figure 2.4. **A)** STEM image of AgNCs, scale bar represents 100 nm, **B)** example gaussian distribution of AgNC size, average edge length 33.3 +/- 4 nm, **C)** UV-Vis spectrum of AgNCs with a peak absorbance at 451 nm.

Section 2.5 Characterization Techniques

This section will describe the methods used to prepare and perform UV-Vis analysis and STEM analysis.

2.5.1 UV-Vis Analysis

The UV-Vis instrument listed **Section 2.1** was used for all analysis. The samples were prepared by diluting 0.5 mL of purified sample with NPW to a final volume of 2 mL. A quartz cuvette was used to scan the sample with the parameters listed in **Table 2.1**. This same method was used for all samples. The sample can be collected after analysis and centrifuged at 11,000 rpm for 15 minutes and then redispersed in NPW to the original 0.5 mL volume.

Table 2.1. Parameters used for UV-Vis analysis.

Parameters used for UV-Vis analysis	
Scan range	1,100 nm to 350 nm
Averaging time	0.02 s
Data interval	1 nm
Scan rate	3000 nm/min
Spectral bandwidth	2.00 nm

2.5.2 STEM Analysis

STEM analysis was done using the instrument listed in **Section 2.1** Before sample preparation all samples were purified a minimum of twice via centrifugation. Typically, 0.5 mL of sample is centrifuged at 11,000 rpm for 15 minutes and the pellet is redispersed in 0.5 mL NPW. The sample is then centrifuged again at 11,000 rpm for another 15 minutes. After the second round of centrifugation the pellet is redispersed in 0.2 mL of NPW. This is done to concentrate the sample to allow for easier STEM analysis.

Once the sample has been properly purified and concentrated approximately 5 µL of the sample is placed onto a STEM grid and left to dry at ambient temperature. The grids used in this work were manufactured by Ted Pella Inc. and were support films, with formvar/carbon with a copper mesh size of 300. The general settings for STEM analysis are listed in **Table 2.2**.

Table 2.2. Parameters used for STEM analysis.

Parameters used for STEM analysis	
Acceleration voltage	30.0 kV
Initial working distance	4.0 nm
Aperture	4
Process time	32 seconds
Scanspeed	8 seconds

Section 2.6 Additional Procedures

This work references samples that underwent additional procedures such as a sodium chloride salt wash or H_2O_2 etching. The procedures for these are described below.

Section 2.6.1 Sodium Chloride Wash

To perform a 'salt-wash' the sample is first purified via centrifugation at 11,000 rpm for 15 minutes. The supernatant is removed, and the pellet is dispersed to the original volume using a saturated sodium chloride solution. The sample is then briefly sonicated and left to sit for 10 to 20 minutes. It is then sonicated once again and centrifuged for 10 minutes at 11,000 rpm. After centrifugation the supernatant is discarded, and the pellet is redispersed to volume with a 1 mM CTAC solution and sonicated briefly. The sample is left to sit for another 10 minutes and then centrifuged for 10 minutes at 11,000 rpm. Once again, the sample is redispersed with 1 mM CTAC and left to sit for 10 minutes.

This is repeated for a minimum of 3 times to ensure that all excess NaCl has been removed. After the final 1 mM CTAC cycle the sample can be redispersed using NPW to either the original volume or a more concentrated volume depending on the required analysis.

Section 2.6.2 Hydrogen Peroxide Etching

To perform further analysis samples were etched with hydrogen peroxide. This was done by taking 0.5 mL of purified sample and 0.5 mL of 3.0 M H_2O_2 and placing them into a centrifuge tube. The solution was inverted to mix and then placed onto a mixer at 400 rpm in ambient conditions for 12-24 hours. After the mixing period the solution was centrifuged at 11,000 rpm for 15 minutes. The supernatant is removed, and the pellet is redispersed with NPW. The sample is then slow centrifuged at 200 rpm for 40 minutes. After the slow centrifugation the supernatant is removed, and the pellet was redispersed with NPW to a final volume of 0.5 mL. The sample was centrifuged a final time at 11,000 rpm for 15 minutes and redispersed using NPW to either the original volume or a more concentrated volume depending on the required analysis.

Chapter 3: Results and Discussion

Section 3.1 Introduction of Galvanic Replacement Reactions

Metal deposition on the nanoscale has been studied significantly in scientific literature.[51-53] Often the interactions of metal onto metal deposition are the primary focus of many of these investigations. Typically, the use of two or more noble metals: Au, Ag, Pd, Pt, etc, are studied for their plasmonic properties mentioned previously. [54,55] The situations examined can vary dramatically as morphologies, sizes, rates, temperatures, reagents, etc are all considered. However, one phenomenon that is prevalent throughout these scenarios is the galvanic replacement reaction briefly discussed in **Chapter 1**.

A galvanic replacement reaction (GRR) occurs when there is a difference in the electrochemical potentials between the two or more metals in question.[46] This difference results in the preferential oxidation of the metal with a lower potential and the reduction of the metal with the higher potential. Often the metal being oxidized is from a bulk solid material and the metal being reduced is in a solution. As the oxidized metal leaves the bulk solid the reduced metal is typically deposited onto the solid material. This ‘exchange’ results in this process being referred to as ‘replacement’.

However, metals have various oxidation states and can undergo reduction/oxidation in various paths and stages, so this is not always an equal ‘exchange’. The wide variance and nature of these galvanic replacement reactions requires detailed study and understanding for each unique situation. Once these system conditions are well understood they can often be manipulated to create tunable, predictable, and repeatable synthetic procedures. Achieving these

tunable procedures is commonly done by controlling, avoiding, or even promoting these conventional galvanic replacement reactions.[56] This work will focus on the conventional galvanic replacement reaction of the gold overgrowth on AgNC followed by its manipulation to control the synthetic process of Au@AgNC formation.

Section 3.2 Conventional Galvanic Replacement Reaction

The system studied in this work focuses on the addition of gold to AgNC. The original AgNC synthesis involves reduction and oxidation reactions but are not the GRR that occurring during the Au overgrowth process. During the original synthesis of AgNCs, $AgNO_3$ serves as the precursor for silver deposition along with the reduction agent L-AA. The Ag (I) from the precursor is reduced by L-AA to Ag (0) which then deposits onto the gold core forming the solid silver. CTAC is included as a capping agent to direct this growth along the (100) facet to create the cubic formation.[22]

During the overgrowth process however, $HAuCl_4$ serves as the gold precursor, where gold is in its Au (III) oxidation state. This gold will then be reduced either by the GRR or a reduction agent. For the scenarios where a reduction agent is included, L-AA is used once again. The gold is eventually reduced to Au (0) by L-AA which then allows for solid gold deposition onto the AgNC. As the gold reduction occurs, Cl^- is released into the system which will favorably form AgCl salt assisting in the preferential oxidation of the Ag atoms. However, in the reactions studied in this work the stochiometric ratios of gold reduction, Cl^- release and silver oxidation are unequal. For each gold atom deposited, three silver atoms are oxidized resulting in

unequal exchange. This creates a form of silver 'etching' from the bulk nanocubes as shown in **Figure 3.1.**

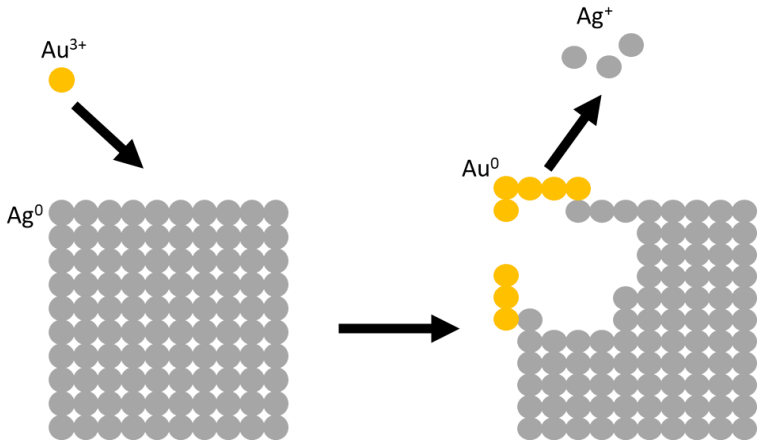

Figure 3.1. Scheme of conventional galvanic replacement reactions.

The oxidation and reduction of the species in this system are driven by the reduction potentials, **Table 3.1** lists out relevant reduction potentials. The higher E_0, value the more favorable the reduction reaction is and more likely it will occur. Looking at **Table 3.1**, the reduction of Au (III) to Au (0) is strongly favorable, allowing for this reaction to occur without much hinderance and thus the promotion of gold deposition. On the opposite end silver reduction is not as favorable and will prefer to undergo oxidation in comparison to gold oxidation, promoting this 'etching'.

Table 3.1 Half-cell reactions of conventional galvanic replacement reactions.[57]

Half Cell Reactions		E_0 (V)
(1)	$AuCl_4^-{}_{(aq)} + 3e^- \rightarrow Au_{(s)} + 4Cl^-{}_{(aq)}$	1.00
(2)	$AgCl_{(aq)} + e^- \rightarrow Ag_{(s)} + Cl^-{}_{(aq)}$	0.223

3.2.1 Gold Overgrowth Procedure

To complete the gold overgrowth of AgNCs the procedure form Mayer et. al. (2017) was adopted with minimal changes and is described below.[32] The procedure described here is for the standard literature-based conditions. In this work different experimental conditions are studied and changes to this procedure will be described in the relevant sections throughout **Chapter 3**.

First, a growth solution was prepared using a scintillation vial. The initial solution contained 0.5 mL of 40 mM CTAC, 0.5 mL of 500 mM L-AA and 1.0 mL of the purified AgNC prepared in **Section 2.4**. The AgNC solution should be sonicated to redisperse any particles that may have settled before use. This solution was capped and placed in an oil bath at 65 ^{0}C while stirring. This solution was allowed to reach temperature before the gold addition step was started.

Next, a 0.125 mM gold solution was prepared by using NPW and $HAuCl_4$ precursor. This solution was mixed well by inversion. A syringe pump was prepared to dispense the prepared gold solution at a rate of 2 mL per hour. After the initial growth solution had reached temperature, it was uncapped and the 0.125 mM $HAuCl_4$ solution was dispensed into the vial via syringe pump while remaining in the oil bath under stirring. This solution was parafilmed during the addition to avoid evaporation.

The volume of 0.125 mM $HAuCl_4$ dispensed will depend on the desired experimental conditions. Using standard literature values this volume is 3.33 mL to obtain Au@AgNCs with an average edge length range of 40 nm depending on the volume of $HAuCl_4$ used for overgrowth. **Figure 3.2 B** provides a plot of average edge length along with a STEM image example. The molar ratios of gold and AgNC are listed in **Table 3.2**.

Once the gold addition was completed the vial was recapped and allowed to stir at 500 rpm and temperature until the solution color was stable and no longer changing. It was then

removed from heat to allow cooling. Depending on the volume of $HAuCl_4$ and the experimental conditions the final solution color may vary dramatically, **Figure 3.3** provides an example of the colors obtained as the $HAuCl_4$ volume changes with all other parameters as described in this section.

The sample was purified via centrifugation at 11,000 rpm for 10 minutes. After centrifugation, the supernatant was removed, and the pellet was redispersed using NPW to a volume of 1 mL. This volume is chosen to keep the initial nanocube concentration the same between the Au@AgNCs and standard AgNCs. It is important to purify the solution within 24 hours of the gold addition. The Au@AgNCs are not stable with excess L-AA and $HAuCl_4$ in solution.

Once the solution is purified it is stable for long periods of time and can be stored at room temperature away from light. A UV-Vis spectrum should be collected using the preparation method described in **Section 2.5.1**. The spectrum obtained will vary on the experimental conditions used, **Figure 3.2 A** shows an example spectrum with varying $HAuCl_4$ at the conditions described above, 65 ^{0}C with an addition rate 2 mL per hour.

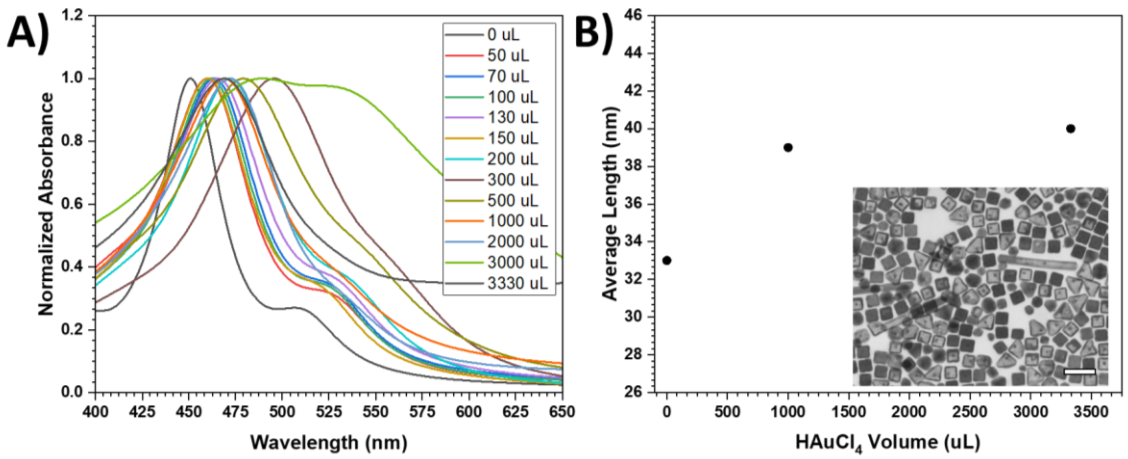

Figure 3.2 A) UV-Vis Spectra of Au@AgNC with varying gold volumes at standard literature conditions, 0.6 mM KI, 65 ^{0}C and an addition rate of 2 mL per hour, **B)** Size plot of Au@AgNC at various gold volume additions, inset STEM image at 1000 µL $HAuCl_4$ addition.

Figure 3.3. Image of synthesized Au@AgNC using standard literature conditions, 2 mL/hr additions rate at 65^{o}C.

Section 3.2.2 Conventional GRR: Results and Discussion

To study this mechanism, the conventional GRR was performed using a similar procedure to that outlined in S**ection 3.2.1**. The procedural changes from **Section 3.2.1** that were made included hand pipetting for quick additions of the gold precursor and ambient room

temperature conditions. Initial experiments were done with various gold precursor addition volumes starting at 50 µL and increasing up to 3,330 µL. As the volume of $HAuCl_4$ increases the amount of gold deposited onto the AgNC should also increase. The ratio of available gold to silver in the starting AgNC will change as well as these volumes increase. **Table 3.2** outlines the amount of gold per AgNC.

Table 3.2 Particle and molar concentrations of Au@AgNC and AgNC

Average AgNC Size (nm)	Total Ag particles per mL	Total Ag particles per AgNC	Moles of Ag per AgNC
32	4.1×10^{10}	1.9×10^{6}	3.2×10^{-18}
40	4.1×10^{10}	3.7×10^{6}	6.2×10^{-18}
Volume of Au^{3+} (uL)	**Moles of Au**	**Au^{3+} to Ag ratio at 32 nm edge length**	**Au^{3+} to Ag ratio at 40 nm edge length**
50	6.3×10^{-9}	2.0×10^{9}	1.0×10^{9}
70	8.8×10^{-9}	2.8×10^{9}	1.4×10^{9}
100	1.3×10^{-8}	4.1×10^{9}	2.1×10^{9}
130	1.6×10^{-8}	5.1×10^{9}	2.6×10^{9}
150	1.9×10^{-8}	6.0×10^{9}	3.1×10^{9}
200	2.5×10^{-8}	7.9×10^{9}	4.0×10^{9}
300	3.8×10^{-8}	1.2×10^{10}	6.1×10^{9}
500	6.3×10^{-8}	2.0×10^{10}	1.0×10^{10}
1000	1.3×10^{-7}	4.1×10^{10}	2.1×10^{10}
2000	2.5×10^{-7}	7.9×10^{10}	4.0×10^{10}
3000	3.8×10^{-7}	1.2×10^{11}	6.1×10^{10}
3330	4.2×10^{-7}	1.3×10^{11}	6.8×10^{10}

UV-Vis analysis is used to monitor the surface plasmon resonance peaks or LSPR of the AgNC and Au@AgNC. The LSPR is a result of the plasmonic behavior displayed by metals on the nanoscale.[48] Each metal will interact with light differently and will therefore have a unique LSPR peak or region. As mentioned in **Section 1.2** this LSPR position is directly dependent on

the shape and structure of the nanoparticle. Silver nanocubes will have a LSPR peak at approximately 440 - 460 nm and gold dominate NCs will display a red shifted LSPR peak at nm, see **Figure 3.4**.

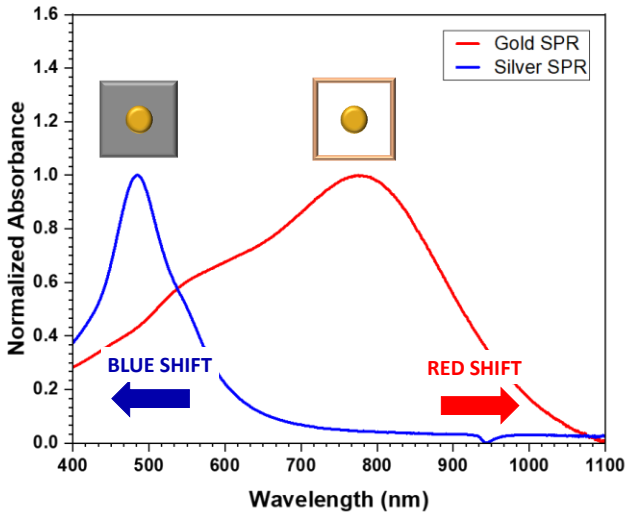

Figure 3.4. Example UV-Vis spectra and typical LSPR peaks for AgNCs and Au@AgNCs.

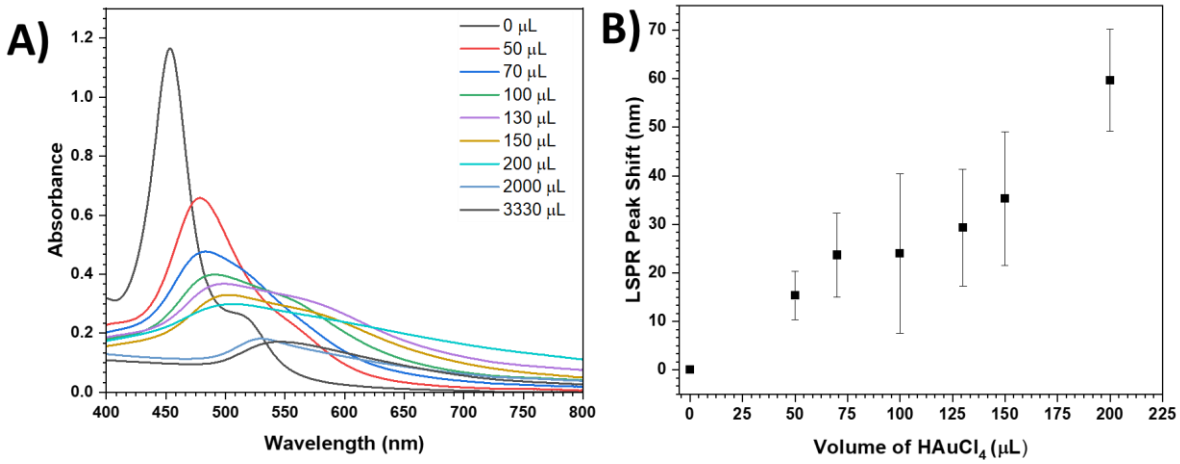

Figure 3.5. **A)** UV-Vis spectra of Au@AgNC at various $HAuCl_4$ addition volumes, room temperature and fast addition, **B)** LSPR peak position plot as the volume of $HAuCl_4$ increases.

Figure 3.5 shows an initial AgNC peak position at 443 nm, 0 µL $HAuCl_4$, followed by a redshift as the $HAuCl_4$ volume increases. The peak position red shifts to 468 nm at 150 µL which is still typically representative of silver LSPR peaks. Once this volume is increased further the peak position is shifted to 513, 576, and 595 nm for 200, 500 and 3330 µL volume addition respectively. These later LSPR peak positions are representative of gold resonance suggesting that once the addition volume surpasses 150 µL there is now enough Au deposited on the AgNC to create a significant LSPR peak. Scanning transmission electron microscopy was then preformed to confirm the observed trend. **Figure 3.6** shows the STEM images for various $HAuCl_4$ addition volumes.

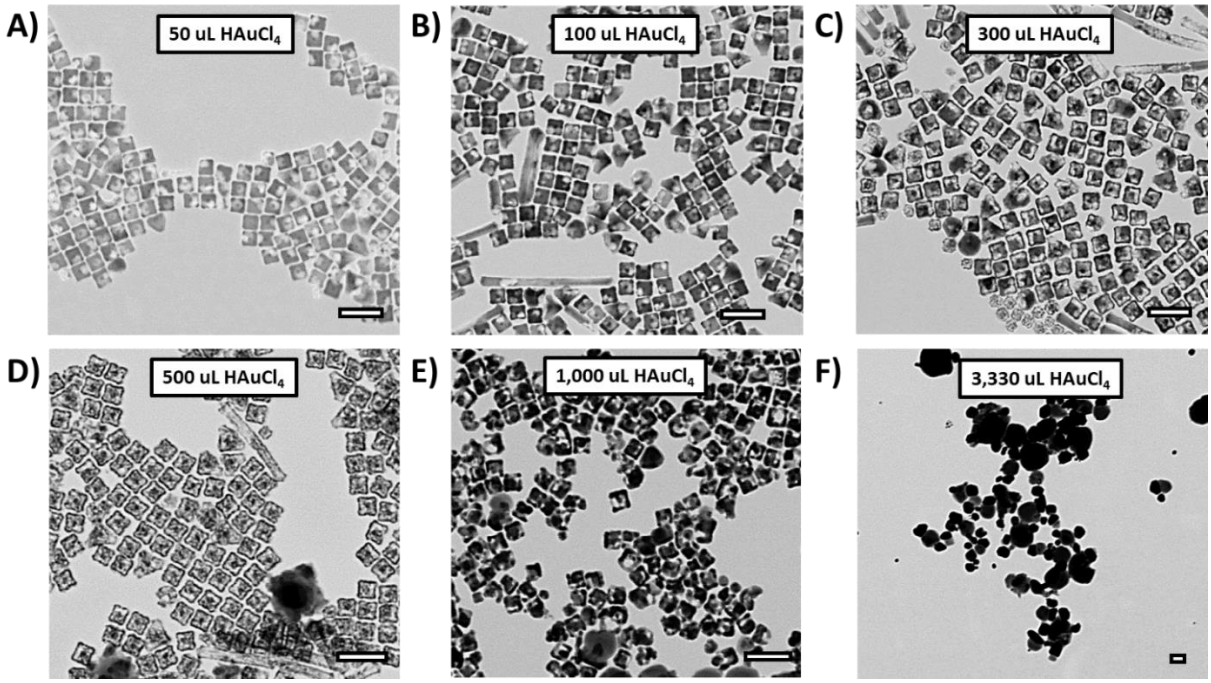

Figure 3.6. STEM images of Au@AgNC synthesized using conventional galvanic replacement reaction mechanisms, at room temperature and quick additions of various $HAuCl_4$ volumes **A - F)** 50 µL, 100 µL, 300 µL, 500 µL, 1,000 µL, and 3,330 µL respectively.

As the volume of gold precursor increases the amount of etching observed in the bulk nanocubes also increases. This is expected as the amount of gold increases the number of free Cl^- also increases resulting in silver oxidation and its displacement from the bulk AgNC. However, as we can see with **Figure 3.6 E** once the volume increases to a certain point the nanocubes lose structure and begin to break apart. Once the volume reaches 3,330 µL the cubic shape is lost entirely become gold aggregations, as seen in **Figure 3.6 F**. These STEM images directly coincide with the observed UV-Vis trends. The higher volume additions lose LSPR peak distinction due to this loss of cubic shape. A proposed scheme for this etching and shape loss is shown in **Figure 3.7.**

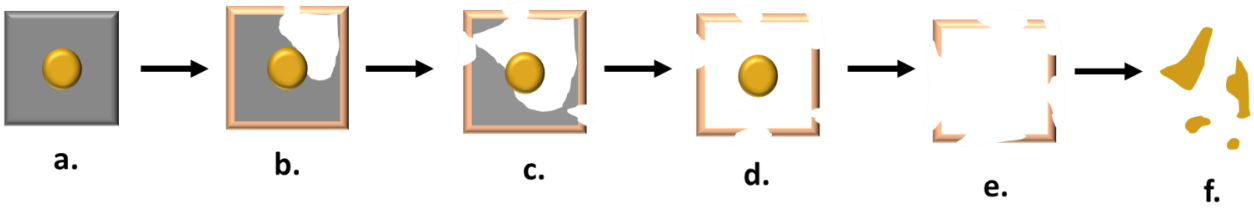

Figure 3.7. Scheme showing the progression of the GRR etching and eventual cubic morphology loss.

As the gold deposition and the silver oxidation begins to occur there are multiple processes that can be observed. Firstly, it is shown that silver will tend to oxidize along edges where previous silver atoms have already been oxidized and etched. This is known as the Kirkendall effect and often observed in nanoparticle behavior.[58] As one metal is diffused or etched away, diffusion rates change to where the newly formed interfaces are more favorable for diffusion. This leads to more vacancies forming along the pervious vacancies.[27] This leads to

larger and larger voids forming rather than a spotted pattern. This is reflected in the STEM images seen in **Figure 3.6 (A-C)** as large voids are present.

Next it is observed that the deposition of gold is not uniform as it builds a layer around the AgNC. **Figure 3.6 D** shows rough and uneven outer gold layers. Although the favorability of silver being reduced back to Ag (0) after oxidation is low, it may still happen in some capacity. If this is the case, then the silver would be deposited onto the outer layer along with the gold. This would result in an alloyed layer composed of both Ag and Au. The presence of an alloyed outer layer adds another component to consider as now the silver in the outer layer could be oxidized again and thus leaving the outer layer. If this is done pinhole like formations would form along the outer layer of the bulk AgNC. These 'pinhole' formations would then allow a spot for the interior silver to escape as it is oxidized. Having a limited number of routes for the silver to leave the bulk cube in conjunction with the Kirkendall effect would ensure the large interior void formations observed.

The formation of alloys can be probed by H_2O_2 washing as described in **section 2.6.2.** Hydrogen peroxide will remove silver as it is susceptible to oxidation from the hydrogen peroxide.[32] If alloys are forming, then the outer shells of the Au@AgNC should reflect this as silver is H_2O_2 washed. **Figure 3.8 A-B** shows conventional GRR nanocubes with a 300 µL addition of $HAuCl_4$ before and after H_2O_2 etching respectively. After H_2O_2 etching the interior of the AgNC is fully etched while the outer layer is not. This suggests that the outer layer of gold is not complete enough to protect the interior bulk silver.

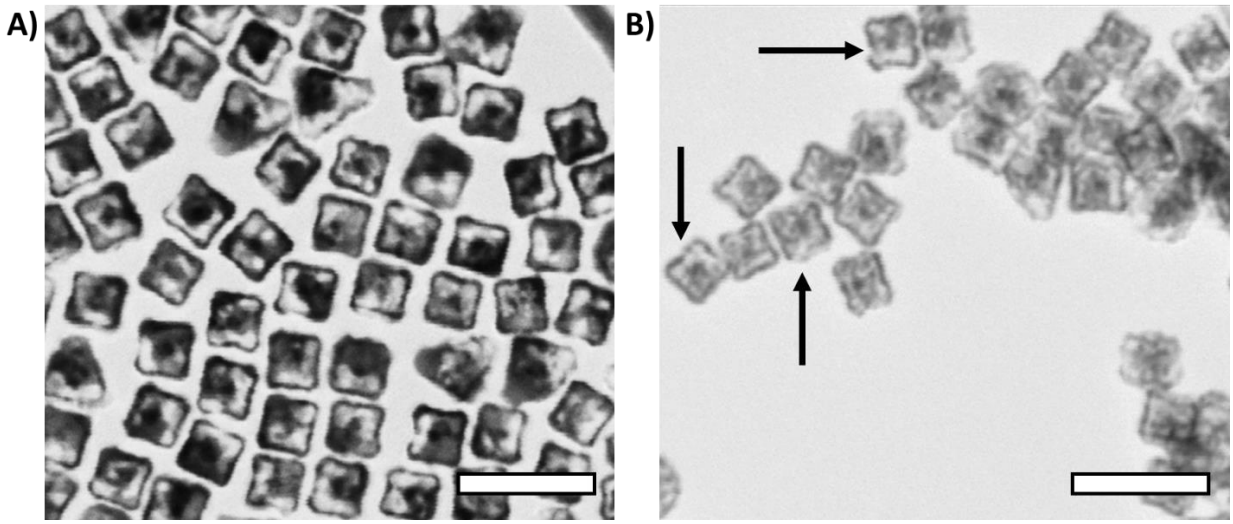

Figure 3.8. STEM images of 300 µL $HAuCl_4$ addition at room temperature with fast addition **A)** before and **B)** after 3.0 M H_2O_2 washing.

As these pinholes continue to get larger the structure of the Au@AgNC eventually becomes compromised and loses stability. These gaps eventually become large enough that the Au core can escape from the cube structure. **Figure 3.6 F** also shows the expected aggregations as the $HauCl_4$ volume is increased further and all cubic structure is lost. It is crucial to maintain both silver interior and the cubic structure as both these factors are what create the ideal plasmonic properties discussed in **chapter 1**.

After an investigation of the conventional galvanic replacement reaction using simplified conditions, room temperature and fast additions, some trends can be concluded. As the silver is oxidized and etched it follows the Kirkendall effect resulting in large interior voids. Some alloy formation is occurring which may be resulting in 'pinhole' formations within the outer shell later. Once the addition of $HauCl_4$ becomes large enough these pinholes become sufficient in size for the Au core to escape and the cubic structure to be lost entirely resulting in gold aggregations.

Section 3.3 Introduction of Reduction Agent

The conventional GRR does not allow full synthetic control over the rate and extent of etching observed in the AgNCs. To gain further control a reduction agent will be included during the synthesis as a means to slow the reduction of Au (III) to Au (0). The reduction agent used in this study is L-AA. This reduction agent was chosen as it is understudied in literature for gold overgrowth process. Literature typically focuses on the polyol process using ethylene glycol as a reducing agent.[60,61] Poly (vinyl pyrrolidone), PVP, is also the most common stabilizing agent used during AgNC synthesis.[62, 63] When buying premade AgNC they are commonly sold in PVP as well, Sigma Aldrich, nanoComposix, Fisher Scientific, and NanoSeedz as few examples.

Ascorbic acid will reduce the gold precursor salt as it is introduced into the system but due to L-AA being a weak reduction agent will not initially reduce Au (III) all the way to Au (0)[59]. Instead, the L-AA will form an intermediate Au (I) state, shown in **scheme 3.1**. The reduction of Au (I) to Au (0) is also more favorable compared to the reduction of Au (III) to Au (0), see **table 3.3**.

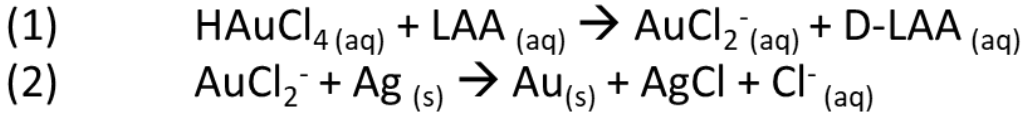

Scheme 3.1. Reaction equations of gold precursor and reduction agent.

Table 3.3 Half-cell reactions of gold precursor and reduction agent, L-AA.[46]

Half Cell Reactions		E_0 (V)
(1)	$AuCl_2^-{}_{(aq)} + e^- \rightarrow Au_{(aq)} + 2Cl^-_{(aq)}$	1.11
(2)	$AuCl_4^-{}_{(aq)} + 3e^- \rightarrow Au_{(s)} + 4Cl^-_{(aq)}$	1.00
(3)	$AgCl_{(aq)} + e^- \rightarrow Ag_{(s)} + Cl^-{}_{(aq)}$	0.223

This Au (I) state is important to the rate of etching as now the exchange for Au and Ag will be one to one. This equal exchange will potentially create less etching showing a strong difference from the conventional GRR. The point at which the nanocubes become hollow or fully etched should also be slower if less etching is occurring. Less pinhole formations and alloying would be expected as less silver is being etched and available for alloy deposition.

Section 3.3.1 Reduction Agent: Results and Discussion

This section uses the procedure described in **section 3.2.1** but at room temperature using fast additions. Initial results showed a significant difference in the colors of the solutions synthesized as $HAuCl_4$ volume increased compared to the conventional GRR. **Figure 3.9 A and B** show the solution colors of the conventional GRR without and the GRR reaction when the reduction agent is included respectively. The color shift is more gradual with the inclusion of reduction agent possibly suggesting that the cube morphology is not changing significantly.

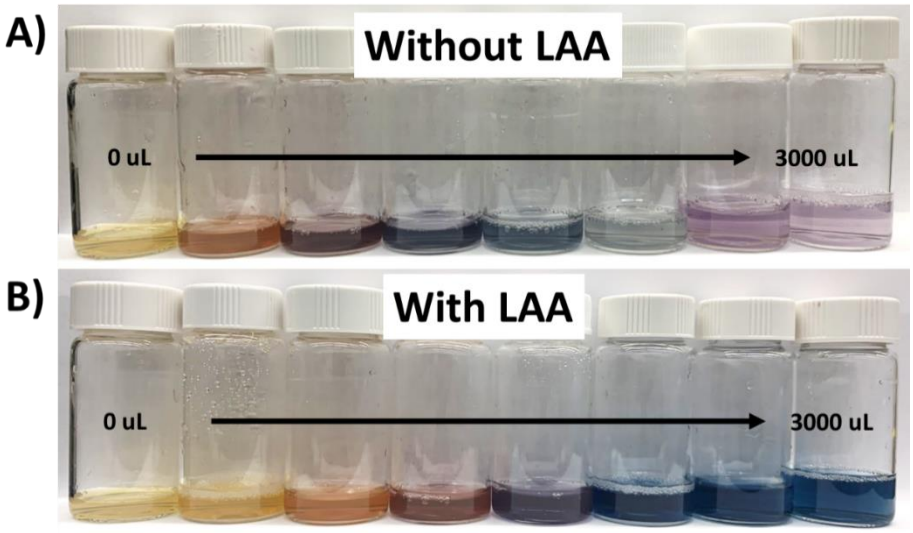

Figure 3.9. Image of solution colors of **A)** conventional GGR and **B)** with L-AA, addition volumes from left to right are. 0, 70, 150, 300, 500, 1000, 2000, and 3000 µL.

UV-Vis analysis maintains peak definition as the volume of $HAuCl_4$ was increased suggesting also suggesting the cubic structure is maintained, see **Figure 3.10 A.** At an addition volume of 100 µL the inclusion of reduction agent minimizes the peak shift to 15 nm while without L-AA at the same volume the peak shift is 37 nm on average. At higher volumes $HAuCl_4$ additions the LSPR peak shifts become more significant. With volume additions ranging from 1,000 µL to 3,330 µL the observed peak shift ranges from 143 to 150 nm from the starting AgNC, **Figure 3.10 B.**

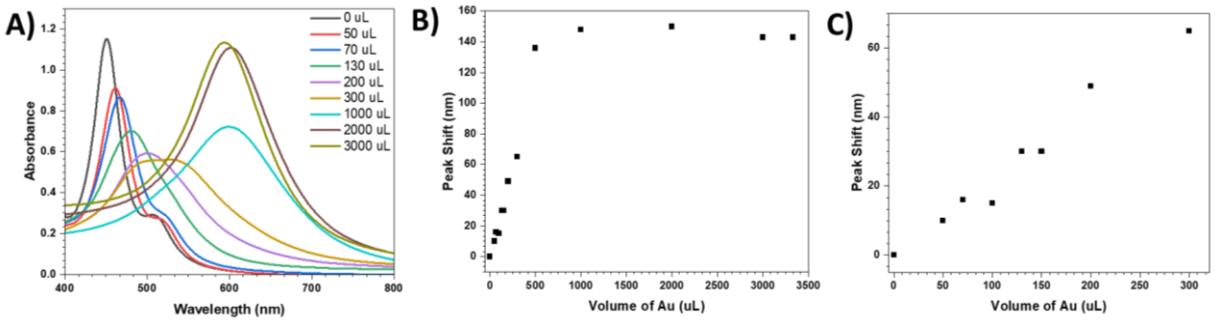

Figure 3.10. A) UV-Vis spectra of Au@AgNC at room temperature, fast addition with L-AA included, **B)** and **C)** LSPR peak shift of the Au@AgNC shown in **A**.

Although shift from the AgNC suggests that the Au@AgNC is mainly Au dominate, the difference in peak shift at the higher volumes is minimal. With an addition of 1000 µL the peak shifts by 148 nm and at a volume of 3000 µL the peak shift is at 143 nm. These close shifts with drastic volume changes suggest that the cube morphology is no longer significantly changing. STEM images were collected to confirm this**,** see **Figure 3.11.**

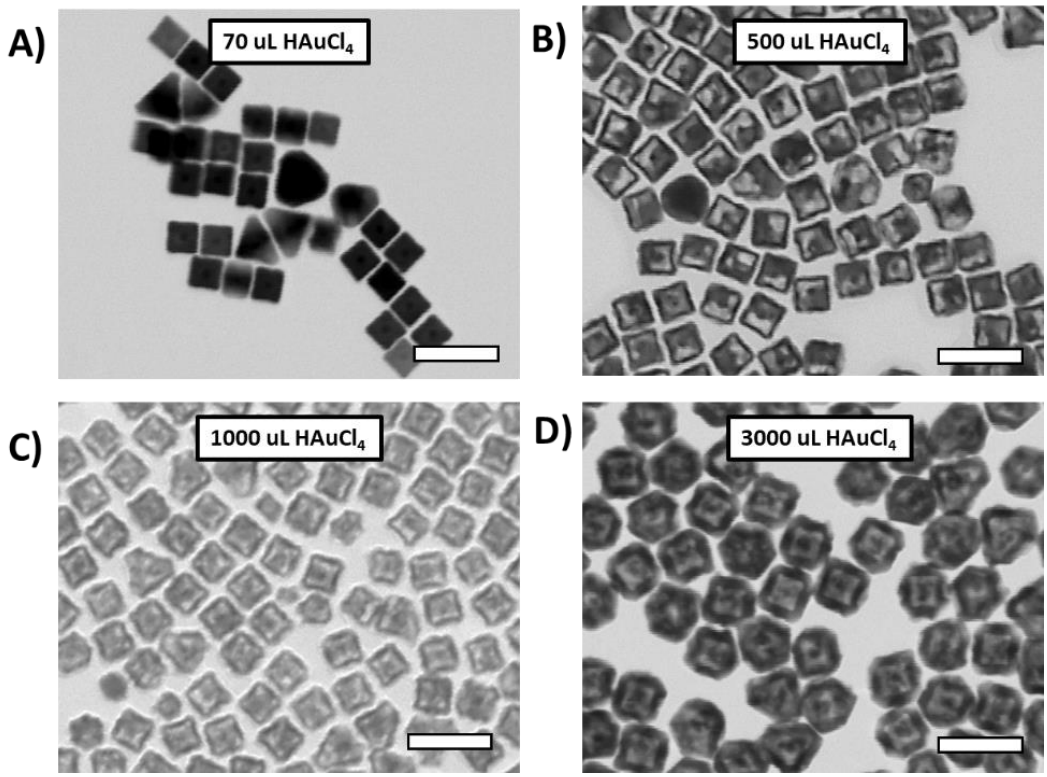

Figure 3.11. STEM images of Au@AgNC at room temperature, fast addition with L-AA included at **A)** 70 µL $HAuCl_4$, **B)** 500 µL $HAuCl_4$, **C)** 1000 µL $HAuCl_4$ and **D)** 3000 µL $HAuCl_4$

The STEM images show major differences from the system without L-AA. Firstly, there is no etching present at the lower addition volumes, 50-70 µL, and there is minimal etching at 100 µL. Without L-AA there was already significant etching at 50 µL, see **Figure 3.11 A.** Secondly, as predicted by the UV-Vis analysis the cubic morphology is maintained at higher addition volumes. Also matching the UV-Vis trends, at higher addition volumes the same amount of etching is observed justifying the similar LSPR peaks, **Figure 3.11 C and D**. Without L-AA at these larger volumes the Au@AgNCs displayed large gaps in their frames or had formed aggregations.

There is also a size difference observed with the presence of L-AA. Without L-AA the average size aftergrowth was 35.4 nm at an addition volume of 500 µL. At the same volume addition, the Au@AgNC average size was 40.5 nm with the inclusion of L-AA.

These experiments have shown that use of L-AA allows for two primary benefits for synthetic control. 1) the ability to maintain cubic morphology at higher gold addition volumes and 2) minimization of the amount of silver that is etched at lower gold addition volumes.

Section 3.3.2 Hexagonal Formations

However, one drawback was observed when L-AA was included in the synthesis, hexagonal formations become present at higher gold addition volumes. A preliminary set of experiments were done to see at which gold addition volume these hexagonal shapes initially appear. Various gold additions between 500 µL and 1000 µL were done using the same synthesis conditions, room temperature and fast addition by hand pipetting. Hexagonal shapes only began to commonly appear once the addition volume reached 800 µL and above, **see Figure 3.12.**

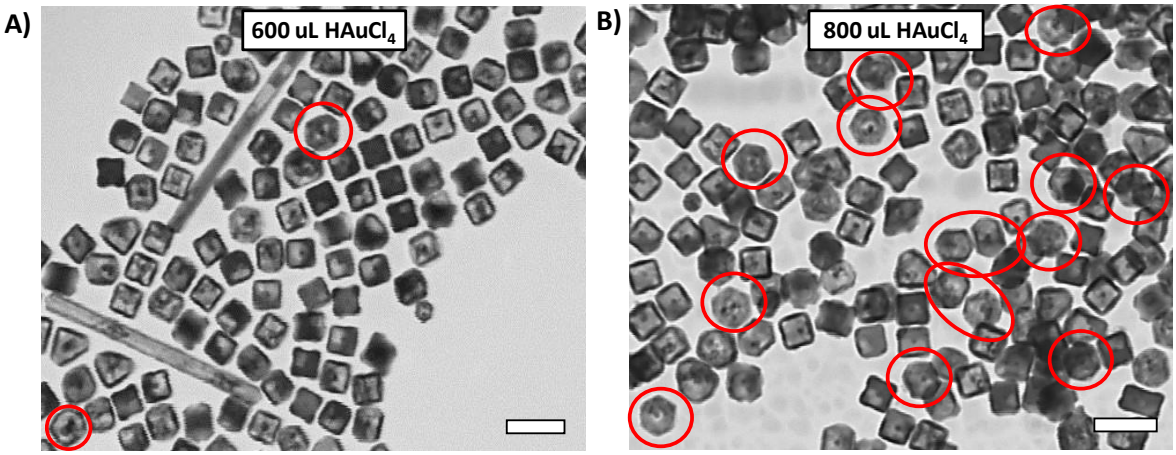

Figure 3.12. STEM images of Au@AgNC at room temperature, fast addition with L-AA included at **A)** 600 µL $HAuCl_4$ and **B)** 800 µL $HAuCl_4$ addition. Hexagonal formations highlighted in red circles.

The appearance of hexagonal shapes provides multiple points of concern if the goal is to gain synthetic control of Au@AgNC formation. Firstly, the hexagonal shape particles are typically fully etched and absent of silver. This is non-ideal as silver is the preferred material for enhanced plasmonic properties. Although the hexagonal morphology increases the number of sides and corners and thus plasmonic hotspots in comparison to a cubic structure, this lack of bulk silver is a major drawback. Secondly, the portion of Au@AgNCs that become hexagonal is not uniform. **Figure 3.12 B** shows this clearly as only a portion of the particles are hexagonal.

Homogeneity needs to be a major concern if repeatable and predictable synthetic control over Au overgrowth is to be achieved. To address the presence of hexagonal shapes two approaches were considered with the intention of avoiding hexagonal formations altogether. The first approach was to slow down the rate of $HAuCl_4$ addition, and the second approach used an increased reaction temperature.

So far, this work has used simplified experimental conditions, room temperature and fast additions, to study the basic mechanisms. Literature, however, often uses slower addition rates via syringe pump to perform gold additions.[32] The use of a syringe pump at an addition rate of 2 mL per hour was then explored to see if synthetic control over the hexagonal formations could be improved.

Using a slower addition rate will affect the system in a couple of beneficial ways. As silver is etched from the bulk NC, AgCl is formed. With a quick addition rate, the oxidized Ag^+ may not have adequate time to find Cl^- ions to form the AgCl salt and may instead be reduced back to Ag (0) allowing for its deposition on the NC once again. As the volume of $HAuCl_4$ introduced is increased the CTAC in solution is not increasing. When the higher addition volumes are compounded with the excess silver redeposition the CTAC in solution may no longer be sufficient to maintain selective growth direction. During Au@AgNC overgrowth the concentration of CTAC in solution is approximately half of that during AgNC synthesis. If this was to be explored then multiple other interactions would have to be studied as the CTAC interacts with the silver, gold and L-AA. This work, however, is focusing on the Ag and Au interactions so this this was not explored further here.

Another benefit of a slower addition rate is allowing more interaction time between the gold precursor and the L-AA in solution. This may allow for a higher percentage of the Au (III) atoms to be reduced to Au (I) before reducing all the way to Au (0) for deposition. This would ideally create a scenario with less silver etching due to even one to one exchange of Au and Ag atoms.

Initial observations of the slower addition rate showed different solution colors than fast additions, suggesting a difference in the cubic morphology, either in shape, size or etching rate**,**

see Figure 3.13 A-B. Analysis via UV-Vis upheld distinct peaks with a significant red shift as Au addition volumes increased suggesting a strong shift towards Au dominate Au@AgNCs and therefore significant etching, Figure **3.13 C.** STEM images however, showed a wider variance in the amount of etching than expected from the UV-Vis spectra.

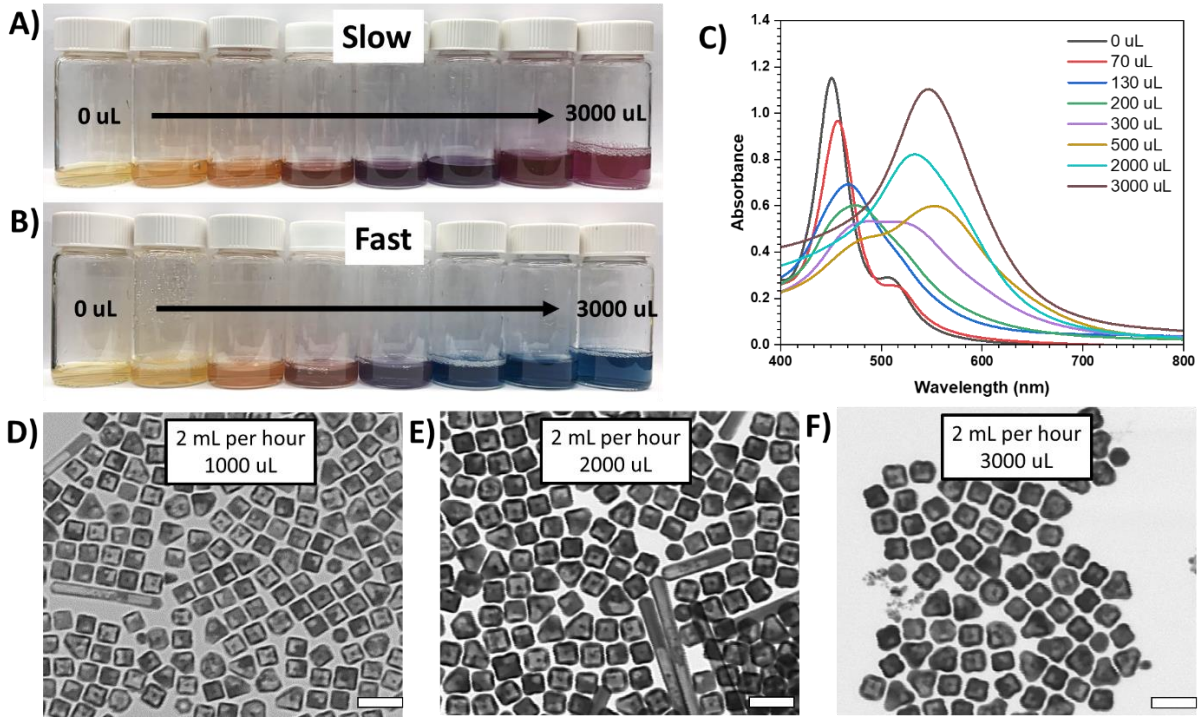

Figure 3.13. A and **B)** solution images of reactions with slow and fast $HAuCl_4$ addition rates respectively, **C)** UV- Vis spectra of Au@AgNC overgrowth at room temperature with a slower addition rate, **D-E)** STEM images of **C** at various addition volumes.

Looking at **Figure 3.13 D-F,** it is shown that the etching rates at all three addition volumes. 1000 µL, 2000 µL and 3000 µL, is inconsistent. Fully etched hollow Au@AgNC are observed as well partially etched Au@AgNCs. However, the percentage of hexagonal formations is reduced significantly. UV-Vis data also shows a strong difference in the LSPR peak shifts

from the starting AgNC. There is less shift observed at a slower addition rate as the Au addition volume increases. This smaller shift is due to better preservation of silver in the bulk NC.

In summary a slower addition rate 1) better preserved the bulk silver, 2) maintained cubic shape at higher addition volumes, and 3) provided LSPR shift that were less red shifted than fast additions.

Next the use of a higher temperature was explored as a method to discourage hexagonal shape formations. The use of higher temperatures will increase AgCl solubility allowing it to remain in solution and helping prevent the possibility of silver reduction back the Au (0). If the system does effectively reduce the amount of silver deposition, then the amount of outer layer alloying should also be reduced. This is an important factor to be aware of as with less alloying the opportunity of pinhole formations will decrease as well.

Initial UV-Vis observations were similar to that observed with a slower addition rate. A smaller LSPR red shift from the original AgNC was observed while maintaining peak distinction. The LSPR peak shifts at higher gold addition volumes were also within 4 nm of each other as the addition volumes exceeded 1000 µL. These trends also agreed with STEM results, **Figure 3.14 D-F.** Higher $HAuCl_4$ volumes did not result in hexagonal formations and maintained cubic morphology. Same as both the slower addition rate and the room temperature situation, the ratio of fully and partially etched Au@AgNC was nonhomogeneous. One explanation of this non uniform etching may be a result of less alloy formation. The reduction of alloying would minimize the number of pinholes forming on the outer surface which will hinder the opportunity for the silver to leave the bulk NC as it is oxidized.

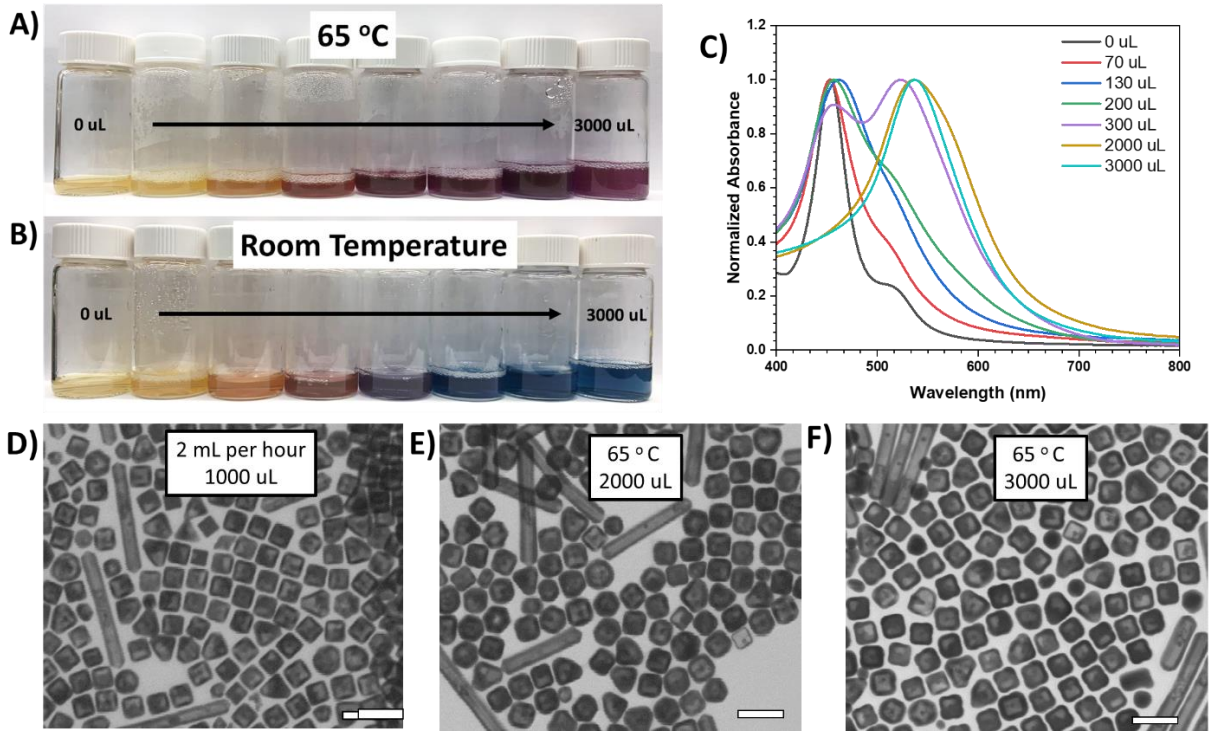

Figure 3.14. A and **B)** solution images of reactions at 65 °C and room temperature respectively, **C)** UV- Vis spectra of Au@AgNC overgrowth at 65 °C temperature with a fast addition rate, **D-E)** STEM images of **C** at various addition volumes.

Section 3.3.3 Hexagonal Formations: Summary

Two approaches were taken as an attempt to prevent the formation of hexagonal morphologies 1) a slower addition rate, 2) increased reaction temperature. Both approaches were successful in avoiding hexagonal morphologies as well as showing a reduced LSPR red shift in comparison to the original AgNC, see **Figure 3.15 A.** These other synthesis conditions also provided more controlled Au@AgNC etching rate at lower $HAuCl_4$ volumes as the peak shifts are smaller representing better-preserved bulk silver, **Figure 3.15 B.** Despite these benefits there is still a need to further investigate synthetic control as the final Au@AgNC morphologies are non-uniform.

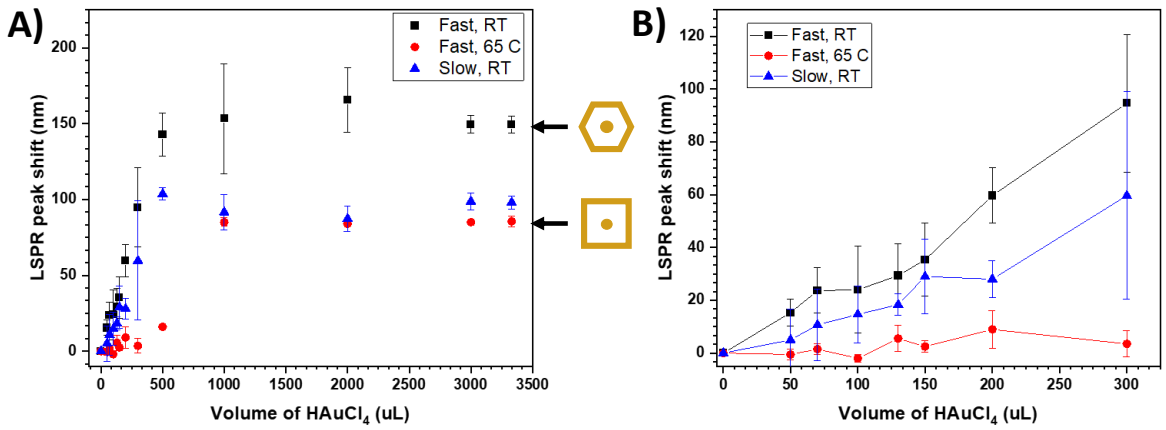

Figure 3.15. A and **B)** LSPR peak shift at various reaction conditions and HAuCl4 addition volumes.

Section 3.4 Introduction of Potassium Iodide

Another method of manipulating these reduction potentials is via the use of potassium iodide, KI. When KI is introduced to the gold precursor new species form resulting in new reduction potentials, see **Scheme 3.2**. Gold will form $AuCl_xI_y$ complexes, where x and y are the ratios of how many chloride ions have been replaced by iodide. This results in reduction potentials ranging from 0.77 -0.33 V depending on the ratio of I to Cl. The reduction potential of AuI_4 is reduced in comparison to $AuCl_4$. This is ideal for creating a situation where the gold will be reduced then deposited at a slower rate, decreasing the number of free ions for silver to interact with. Ideally, this will then result in less etching from the original AgNCs. If this principle is true under experimental conditions, the deposition of gold onto AgNCs might become a predictable tunable factor allow for the synthesis of either etched Au@AgNC or filled Au@AgNCs structures.

(4) $3Ag_{(s)} + AuI_4^-{}_{(aq)} \rightarrow Au_{(s)} + 3AgI_{(aq)} + I^-_{(aq)}$

Half Cell Reactions		E_0
(5)	$AuI_4^-{}_{(aq)} + 3e^- \rightarrow Au_{(s)} + 4I^-_{(aq)}$	0.56
(6)	$AgI_{(aq)} + e^- \rightarrow Ag_{(s)} + I^-_{(aq)}$	-0.152

Scheme 3.2. 4) Reactions of silver nanocubes with gold iodide, **5-6)** half-cell reactions and reduction potentials of $AuIl_4$ and AgI.[28]

This work has shown so far that slight synthetic control can be gained over the formation of Au@AgNC at lower addition volumes of $HAuCl_4$. This is accomplished by both the inclusion of a reduction agent and the use of preferential experimental parameters, such as heat and slower addition rate. However, the final Au@AgNC morphology and dominance of the conventional GRR are non-uniform or tunable as the amount of $HAuCl_4$ increases. Without reduction agent the Au@AgNC loses shape entirely at higher addition volumes. With fast addition rates or ambient temperatures, the Au@AgNC form hexagonal shapes. This amplifies difficulties in analysis, applications and repeatability creating a need for further synthetic control. One way to possibly gain more control is to manipulate the relevant reduction potentials and GRR favorability more so than just the inclusion of a reduction agent as seen in the previous sections.

Potassium iodide (KI) will be introduced into this system in efforts to improve this synthetic control. When KI and the gold precursor interact the Cl^- from the HAuCl4 will exchange for I^- forming $HAuI_4$, see **Scheme 3.2**. The number of chlorine atoms replaced by iodide atoms is dependent on the molar ratio of the two compounds in solution forming. This can lead to complex ranging in molar ratios, $HAuCl_xI_y$. Literature has used various molar ratio often

without full exchange of Cl for I.[32,64] For this work the concentration of KI used to create these new precursor species was 0.6 mM KI. This was done to ensure that the KI is in excess to allow complete exchange to create $HAuI_4$.

This anion exchange to $HAuI_4$ results in a decrease in the favorability of reduction of Au (III) to Au (0). Although the favorability of Au reduction is decreased, it still maintains a higher reduction potential than Ag reduction. The slower reduction of Au will ideally result in a more uniformed deposition of Au shell around the AgNC. However, as expected the relevant reduction potentials involving Ag will also change with the introduction of I. Both the inclusion of the reduction agent and a slower addition rate improved uniform and controlled Au deposition onto the AgNC, so in conjunction with the new $HAuI_4$ complex synthetic control should improve even further.

Section 3.4.1 Potassium Iodide: Results and Discussion.

The procedure used for this section follows that described in **section 3.2.11** but without the use of a heated oil bath. The slower addition rate was used while at room temperature to allow comparison to the system without KI. Initial solution color observation suggested that the shift towards Au dominate Au@AgNCs was faster and less gradual than in the absence of KI. **Figure 3.16 A** shows that there is minimal color shift initially then a significant difference once the addition volume reaches 300 µL and beyond. This is reflected in the UV-Vis spectra as the LSPR peak maintains minimal red shift at lower $HAuI_4$ volumes followed by significant red shift above 1000 µL, see **Figure 3.16 B** and **C**. Once higher additions volumes are reached the peak sharpness is lost as well suggesting either a loss in Au@AgNC morphology or non-uniform etching/deposition behavior.

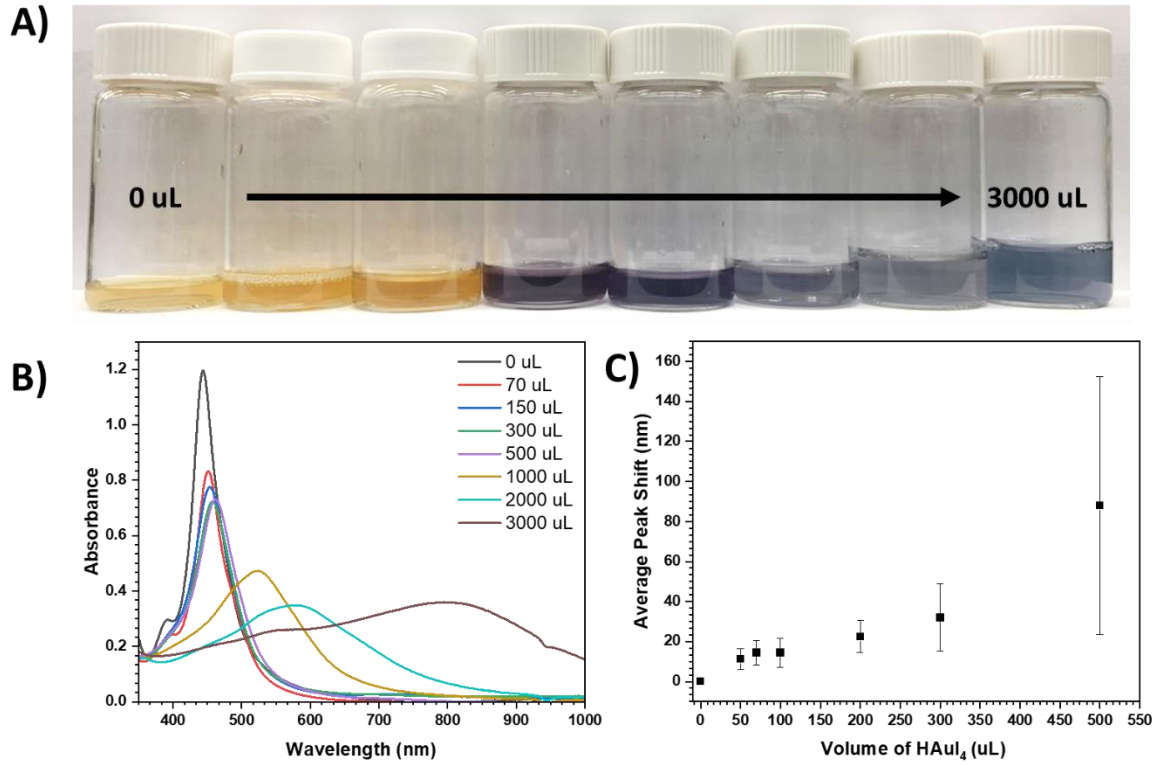

Figure 3.16. A) solution images of as $HAuI_4$ overgrowth at room temperature with a 2 mL per hour addition rate, **B)** UV- Vis spectra of **A** and **C)** LSPR peak shift of **A**.

Via STEM analysis is was shown that both 50 µL and 300 µL addition volumes were fully filled Au@AgNC with minimal Au shell thickness, agreeing with the minimal LSPR redshift, Figure **3.17 A and B**. At addition volumes of 1000 µL mixed etching is observed with some Au@AgNC fully hollow and others only partially, **Figure 3.17 C.** The average Au@AgNC size also increase as more $HAuCl_4$ is introduced. At 50 µL, 200 µL, 500 µL, and 1000 µL the average Au@AgNC size is 32.6 ± 1.5 nm, 33.0 ± 2.9 nm, 33.1 ± 2.9 nm, 38.7 ± 2.8 nm respectively.

Increasing the addition volume even further results in fully hollow Au@AgNC, **Figure 3.17 D**. However, these fully hollow NCs display various nonuniform outer layer deposits and

shell thickness. The absence of the Au core is also observed at these higher addition volumes suggesting that the shell formed pinholes large enough for the Au core to escape, **Figure 3.17 E** and **F**. This escaped core in conjunction with the etched silver may be the sources of the extra deposits observed.

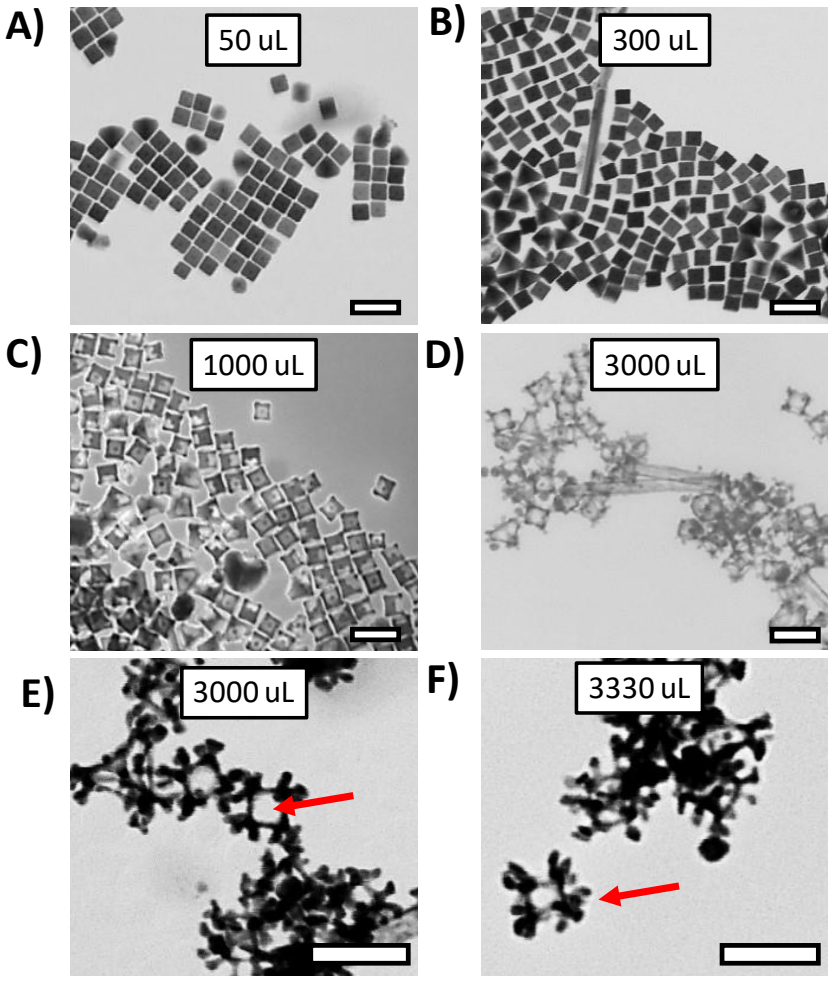

Figure 3.17. A – D) STEM images of $HAuI_4$ overgrowth at room temperature with a 2 mL per hour addition rate at various volumes **E)** STEM image highlighting the absence of Au core and **F)** STEM image highlighting uneven shell deposition.

To investigate the Au shell hydrogen peroxide etching was done as described in s**ection 2.6.2. Figure 3.18** shows the STEM images before and after H_2O_2 etching and washing of 50 µL and 300 µL. With $HAuI_4$ addition volume of 50 µL the cube shape is lost entirely after H_2O_2 etching. It is possible that this total loss of cubic morphology is a result of the Au shell layer being too thin to protect the bulk interior silver. It is also possible that at these lower additions the amount of Au deposited is too small to form a full shell around the AgNC.

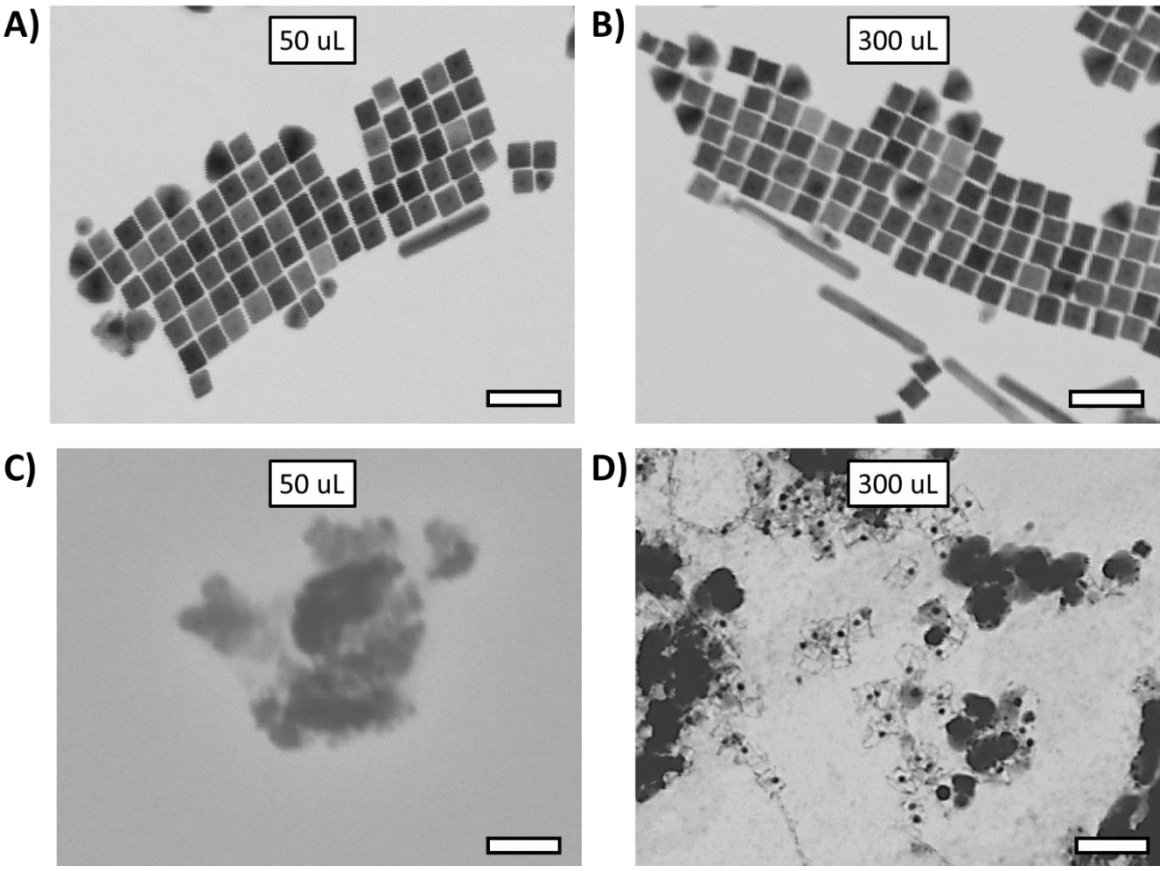

Figure 3.18. STEM images of **A and C)** before H_2O_2 etching and **B and D)** after H_2O_2 etching, of $HAuI_4$ overgrowth at room temperature with a 2 mL per hour addition rate

Repeatability also becomes an issue as $HAuI_4$ addition volumes increase. **Figure 3.19** shows the average shift in LSPR peak position along with the associated error bars for a set of eight trials. At lower addition volumes the errors are relatively small compared to the total shift, within 5-7 nm. However, at higher volumes this error becomes as large as 64.5 nm. This lack of repeatability is a significant issue for synthetic control. STEM images support this increased variability as addition volumes increase. Both uniformly fully filled Au@AgNC and partially or fully etched Au@AgNCs have been observed at addition volumes of 500 µL, **see Figure 3.19 A and B** respectively. **Figure 3.19 D and E** shows non-uniform varied etching for one trail while uniform complete etching has been observed for other trials with 1000 µL of $HAuI_4$. This wide variance in morphologies and etching is also reflected in the UV-vis spectra as shown in **Figure 3.19 C and F**. The LSPR peak for 1000 µL addition trail #4 is blue shifted compared to trial #2, matching the presence of more silver seen in the STEM images, shown in **Figure 3.19.**

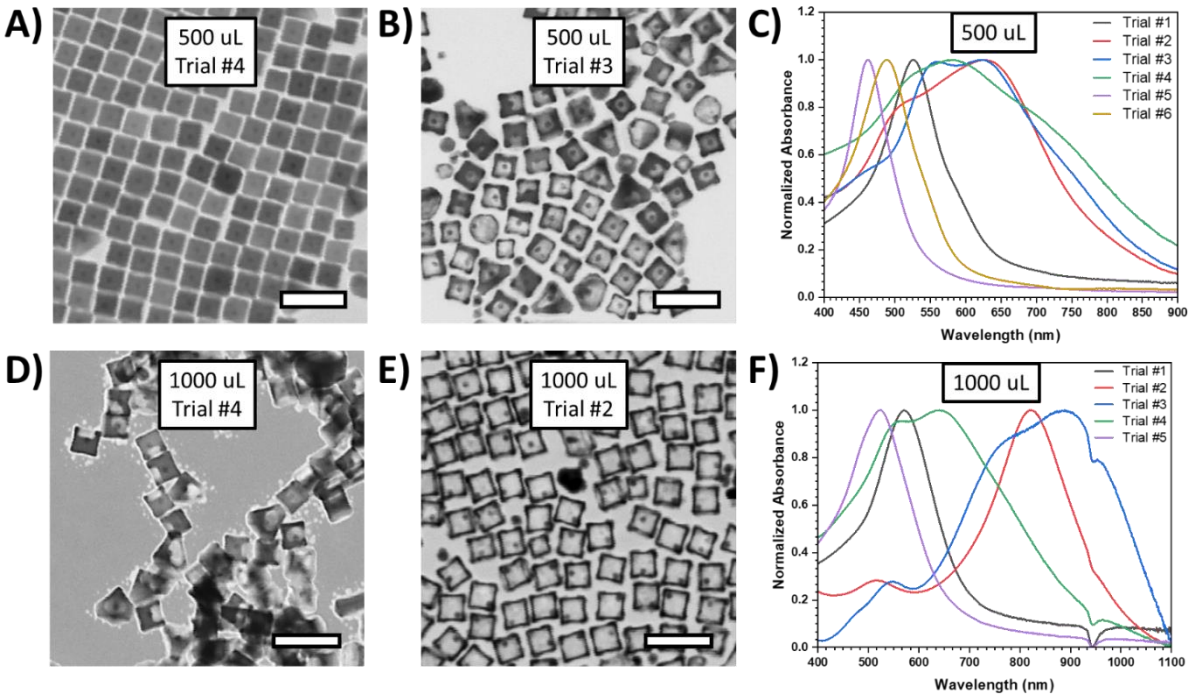

Figure 3.19. STEM images of $HAuI_4$ addition trials at different volumes **A, B)** 500 uL and **D, E)** 1000 uL. **C, F)** UV-Vis plot of various trials of 500 uL and 1000 uL additions.

Lower volume additions not only maintain more repeatability than higher volumes, but they also display stronger impact over the conventional GRR. The LSPR shift of the Ag peak is very similar between the $HAuCl_4$ and $HAuI_4$ systems at low addition volumes, 5.15 nm difference on average for 50-300 µL additions, see **Figure 3.20**. However, when the Au peak is considered the $HAuI_4$ hinders is appearance. When $HAuCl_4$ serves as the precursor the Au peak begins to appear at addition volumes of 300 µL and above. However, this Au peak is not prominent in the $HAuI_4$ system until approximately 1000 µL additions and above. The difference in LSPR behavior is a direct result of the Au@AgNC morphologies.

Minimal addition volumes 50 µL the Au@AgNC morphologies are the same for both with and without KI introduction, **Figure 3.20 A-C**. At addition volumes of 200 µL and above a difference the GGR and etching occurring begins to show. Voids can be seen in **Figure 3.20 D** but when $HAuI_4$ is used no voids are observed, **Figure 3.20 E**. The UV-Vis peak at this volume for the $HAuCl_4$ system is also more broad resulting from the mixture of morphologies. The same observations hold true at 300 µL, **Figure 3.20 G - I.** Once the volume increases beyond this the repeatability issues and various morphologies in the $HAUI_4$ system mentioned above begin making comparison of the LSPR peak shifts difficult.

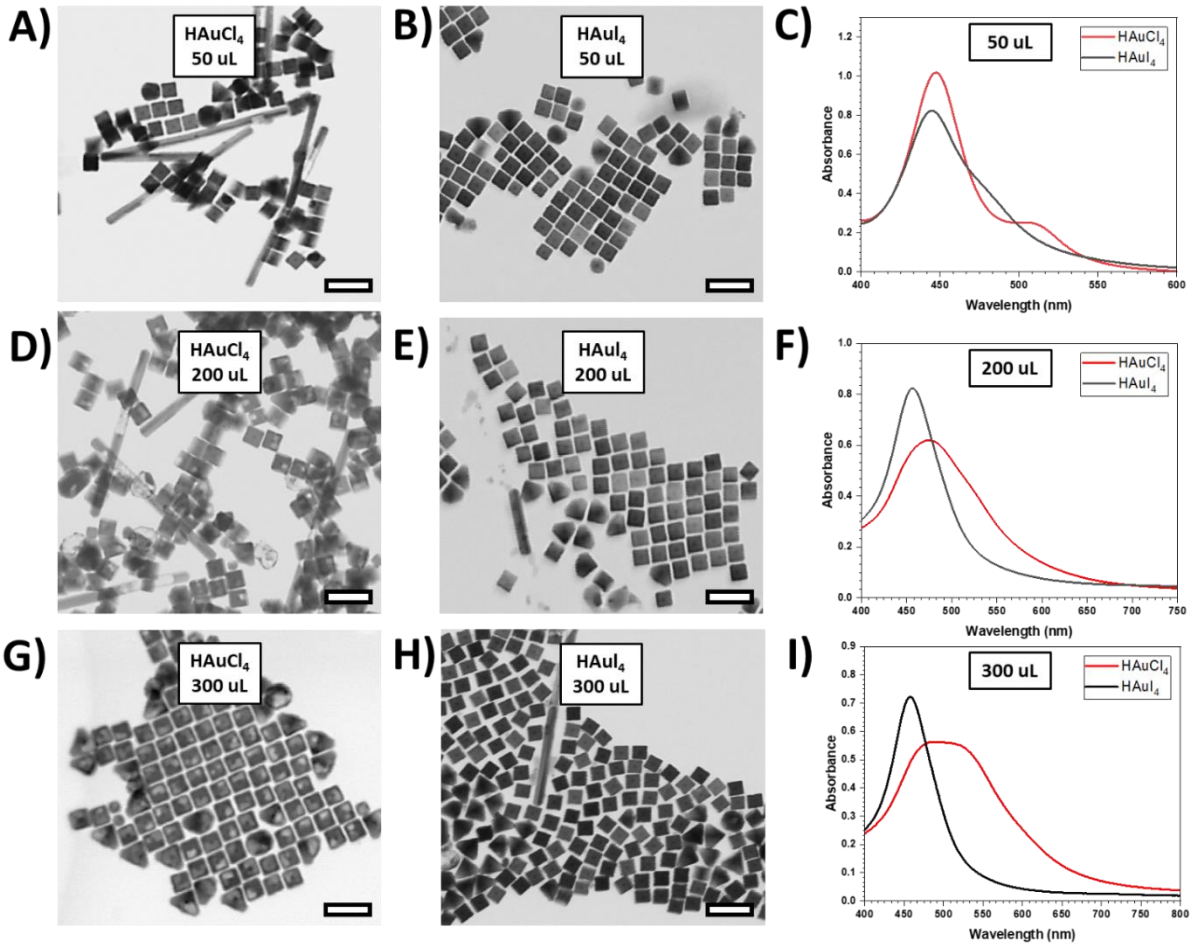

Figure 3.20. A, D, G) STEM images of $HAuCl_4$ overgrowth at room temperature with an addition rate of 2 mL per hour, **B, E, F)** STEM images of $HAuI_4$ overgrowth at room temperature with an addition rate of 2 mL per hour **C, F, I)** UV-Vis spectra of $HAuCl_4$ and $HAuI_4$ comparison at various addition volumes.

With the absence of voids and etching in the STEM images and the preservation of the silver LSPR peak, it has been shown that at lower addition volumes $HAuI_4$ is effective in suppressing the GRR. Larger addition volumes are more complicated as repeatability is not as

high and LSPR peak shape is lost. To address this, the use of increased temperature and $HAuI_4$ as a precursor was investigated.

Section 3.4.2 Potassium Iodide at 65 ºC

So far, this work has concluded that the use of higher temperatures improved repeatability with $HAuCl_4$ as the precursor as well as maintaining cubic morphology. This section will explore if that same improvement holds true with $HAuI_4$ as the precursor. The synthesis is as described in **section 3.2.1.**

At room temperature the use of $HAuI_4$ had minimal LSPR peak shift and repeatable results at addition volumes below 500 µL. This trend was maintained with the use of the increased temperature as shown in **Figure 3.21**. Once this volume is exceeded beyond 300 µL differences are observed. **Figure 3.21** also shows a clear LSPR peak shift difference at 500 µL between the two precursors. Increased temperature has far less significant red shift, remaining within 27 nm of the original AgNC, while at room temperature it was more than three times as strong of a red shift. Repeatability is also shown to be improved with the use of temperature at 500 µL addition.

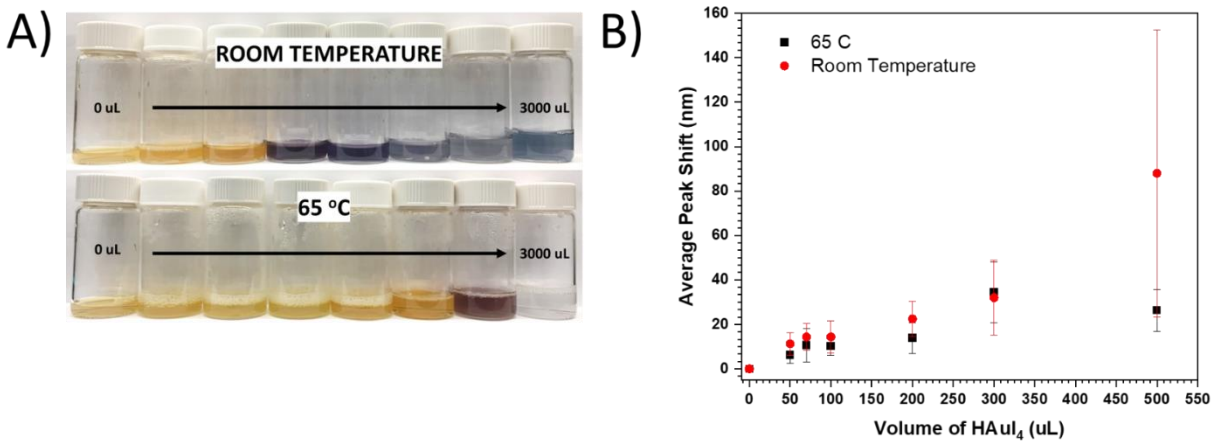

Figure 3.21. A) Picture of experimental solution colors, **B)** LSPR peak shift plot of $HAuI_4$ additions at different temperatures.

The smaller red shift is also observed beyond addition volumes of 500 µL. The silver LSPR peak remains dominant even as the addition reaches 3000 µL. The UV-Vis spectra of the increased temperature with $HAuI_4$ precursor is shown in **Figure 3.22**. Here is clearly seen that the silver peak is still dominate even at 3330 µL. This is a significant difference than what is observed at room temperature. A comparison of the higher volume additions at room temperature vs 65 ^oC are shown in **Figure 3.22 B.** The gold peak does not become prominent at 65 ^oC at the highest addition volumes suggesting that the Au@AgNC maintain the interior Ag. However, when STEM analysis was performed the Au@AgNCs showed a consistent but non-uniform mixture of morphologies. Both fully hollow and fully filled Au@AgNCs were observed from STEM analysis, see **Figure 3.22**. The increased temperature better maintains the original AgNC looking at **Figure 3.22**.

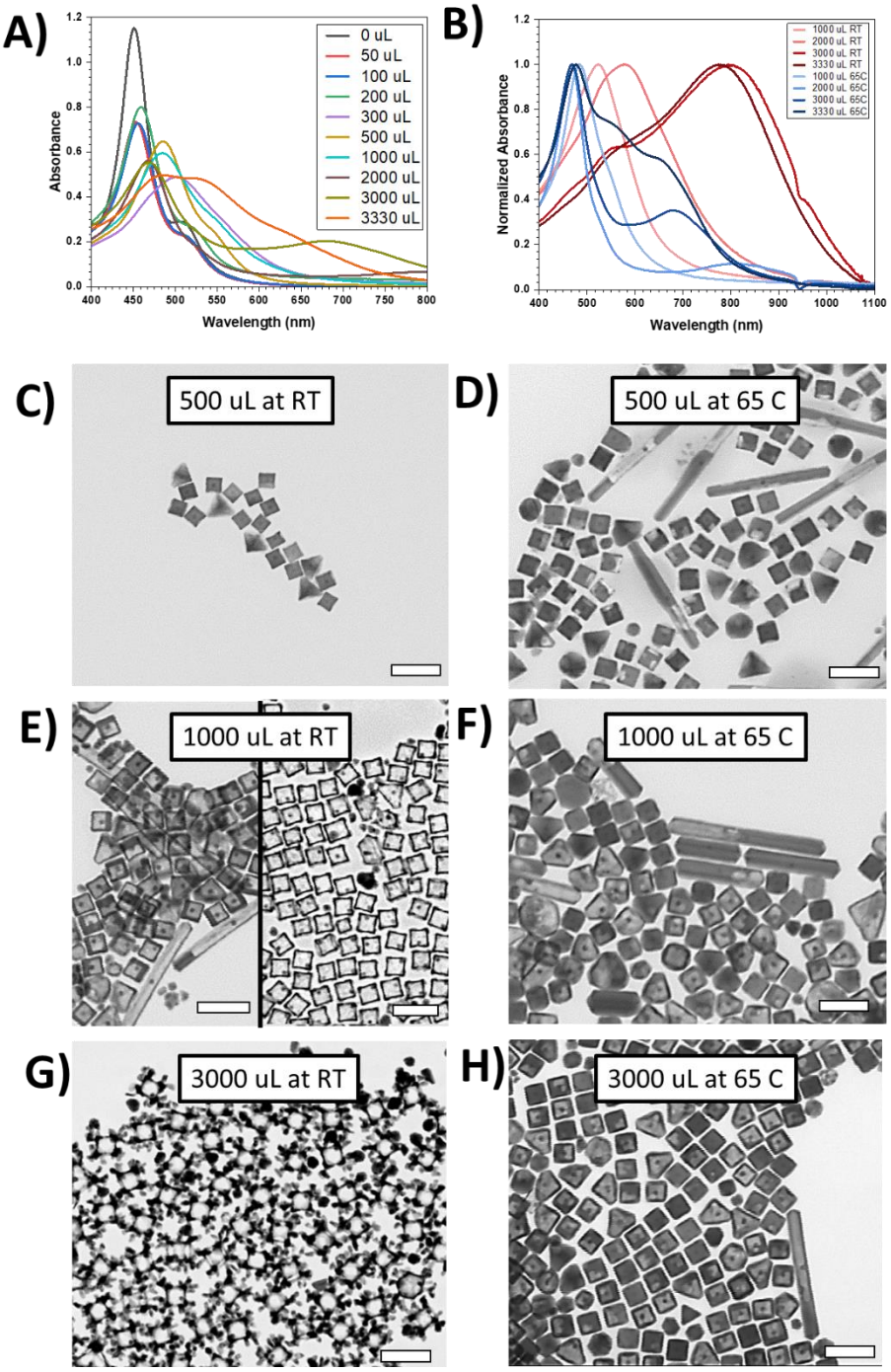

Figure 3.22. A) UV-Vis spectra of $HAuI_4$ addition at 65 ^{0}C with an addition rate of 2 mL/hr. **B)** Comparison UV-Vis spectra of $HAuI_4$ addition at 65 ^{0}C and room temperature with an addition rate of 2 mL/hr. **C, G, E)** STEM images at room temperature, **D, F, H)** STEM images at 65 ^{0}C.

The better preservation of the Ag at an increased temperature could be the result of a couple different factors. As mentioned in the previous section, at higher temperature the Ag salt species that form are more soluble. Increased solubility reduces the likely hood that Ag will be reduced to Ag (0) again and then deposited onto the outer layer. These more soluble Ag salts may also explain why the large masses deposited onto the outer Au@AgNC shell are not observed at 65 ^{o}C as they are at room temp**, Figure 3.22**.

This solubility factor will also minimize the formation of an alloyed outer shell in turn creating more difficult pinhole formation. This would also prevent the Au core from escaping the interior as observed at room temperature. Without these 'pinholes' it is difficult for the kirkendall effect to progress and the bulk Ag to leave the NC.

Hydrogen peroxide etching was done to further investigate the gold shell formation. An addition volume of 50 µL H_2O_2 etching resulted in lose cubic shape entirely suggesting that the amount of gold deposited is not sufficient to protect the interior silver, see **Figure 3.23**. However, at a volume of 500 µL gold shell frames are maintained entirely after H_2O_2. Despite the presence of the gold frame all interior silver has been etched. This means that the gold shell is poupous enough allowing the oxidation and removal of silver by H_20_2 or that the shell consisted of some silver-gold alloying then allowing silver oxidation and removal.

When higher $HAuI_4$ addition volumes were investigated via H_2O_2 different behavior was displayed. At a volume of 3000 µL after H_2O_2 the silver is completely preserved, **Figure 3.23**. This suggests that at this volume the deposited shell of gold is non-porous and thick enough to sufficiently protect the interior silver. To test this further a second wash of H_2O_2 was done along

with two washes with twice the concentration of H_2O_2. Under all conditions the silver was preserved, **Figure 3.23**.

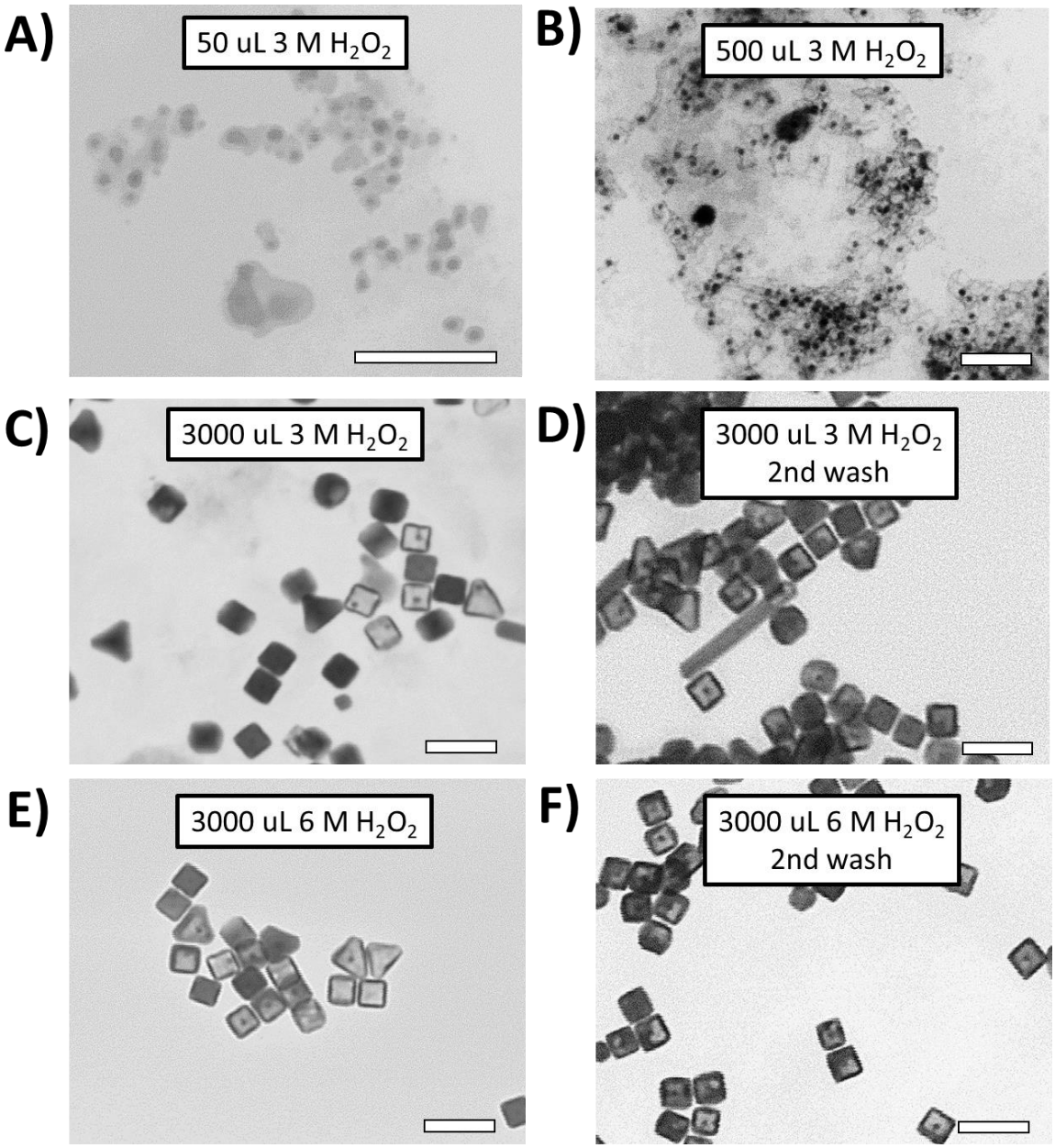

Figure 3.23. STEM images of various $HAuI_4$ volume additions after H_2O_2 etching, reaction conditions, 65 ^oC, 2 mL per hour addition rate.

Section 3.4.3 Potassium Iodide at 65 ºC Conclusion

The use of an elevated temperature, 65 ^{o}C, a slower addition rate and $HAuI_4$ as the precursor salt has allowed for synthetic control and silver preservation at lower addition volumes. At higher addition volumes silver preservation and repeatability are also both increased compared to the other scenarios in this work so far. Nonhomogeneous etching remains an issue however as both fully filled and fully hollowed Au@AgNC are formed from this synthesis method.

Chapter 4

4.1 Conclusion

The synthetic control over Au@AgNC formation is difficult due to the favorability and dominance of galvanic replacement reactions (GRR). This work investigated experimental parameters in efforts to manipulate the reduction potentials in order to control to dominance of the GRR. The use of a reduction agent effectively minimizes the GRR at lower volumes of gold additions but lose cubic shape as these volumes increase. Hexagonal shapes begin to form but this can be avoided with the use of an increased reaction temperature and slower addition rate. Changing the gold precursor from $HAuCl_4$ to $HAuI_4$ manipulates the reduction potential effectively hindering the GRR at higher volumes of gold addition. However, the synthesized Au@AgNC result in nonuniform etching rates.

Works Cited

1) Kim, S.; Kim, J.-M.; Park, J.-E.; Nam, J.-M. Nonnoble-Metal-Based Plasmonic Nanomaterials: Recent Advances and Future Perspectives. *Advanced Materials* **2018**, *30* (42), 1704528. https://doi.org/10.1002/adma.201704528.

2) Prodan, E.; Radloff, C.; Halas, N. J.; Nordlander, P. A Hybridization Model for the Plasmon Response of Complex Nanostructures. *Science* **2003**, *302* (5644), 419–422. https://doi.org/10.1126/science.1089171.

3) Park, G.; Lee, C.; Seo, D.; Song, H. Full-Color Tuning of Surface Plasmon Resonance by Compositional Variation of Au@Ag Core–Shell Nanocubes with Sulfides. *Langmuir* **2012**, *28* (24), 9003–9009. https://doi.org/10.1021/la300154x.

4) Dass, M.; Kuen, L.; Posnjak, G.; Burger, S.; Liedl, T. Visible Wavelength Spectral Tuning of Absorption and Circular Dichroism of DNA-Assembled Au/Ag Core–Shell Nanorod Assemblies. *Materials Advances* **2022**, *3* (8), 3438–3445. https://doi.org/10.1039/d1ma01211h.

5) Chateau, D.; Liotta, A.; Vadcard, F.; Navarro, J. R. G.; Chaput, F.; Lermé, J.; Lerouge, F.; Parola, S. From Gold Nanobipyramids to Nanojavelins for a Precise Tuning of the Plasmon Resonance to the Infrared Wavelengths: Experimental and Theoretical Aspects. *Nanoscale* **2015**, *7* (5), 1934–1943. https://doi.org/10.1039/c4nr06323f.

6) Sui, M.; Kunwar, S.; Pandey, P.; Lee, J. Strongly Confined Localized Surface Plasmon Resonance (LSPR) Bands of Pt, AgPt, AgAuPt Nanoparticles. *Scientific Reports* **2019**, *9* (1), 16582. https://doi.org/10.1038/s41598-019-53292-1.

7) Jana, J.; Ganguly, M.; Pal, T. Enlightening Surface Plasmon Resonance Effect of Metal Nanoparticles for Practical Spectroscopic Application. *RSC Advances* **2016**, *6* (89), 86174–86211. https://doi.org/10.1039/c6ra14173k.

8) Jain, P. K.; Huang, X.; El-Sayed, I. H.; El-Sayed, M. A. Noble Metals on the Nanoscale: Optical and Photothermal Properties and Some Applications in Imaging, Sensing, Biology, and Medicine. *Accounts of Chemical Research* **2008**, *41* (12), 1578–1586. https://doi.org/10.1021/ar7002804.

9) R. Daniel, J.; McCarthy, L. A.; Ringe, E.; Boudreau, D. Enhanced Control of Plasmonic Properties of Silver–Gold Hollow Nanoparticles *Via* a Reduction-Assisted Galvanic Replacement Approach. *RSC Advances* **2019**, *9* (1), 389–396. https://doi.org/10.1039/c8ra09364d.

10) Choi, J.; Han, D.-W.; Song, H.; Lee, D.-H.; Kim, K. Current Achievements of Nanoparticle Applications in Developing Optical

11) Zou, M.; Dong, M.; Zhao, T. Advances in Metal-Organic Frameworks MIL-101(Cr). International Journal of Molecular Sciences 2022, 23 (16), 9396. https://doi.org/10.3390/ijms23169396.

12) Hu, Y.; Jia Xuan Liao; Wang, D.; Li, G. Fabrication of Gold Nanoparticle-Embedded Metal–Organic Framework for Highly Sensitive Surface-Enhanced Raman Scattering Detection. 2014, 86 (8), 3955–3963. https://doi.org/10.1021/ac5002355.

13) Zhang, Y.-J.; Chen, S.; Radjenovic, P. M.; Nataraju Bodappa; Zhang, H.; Yang, Z.; Tian, Z.-Q.; Li, J. Probing the Location of 3D Hot Spots in Gold Nanoparticle Films Using Surface-Enhanced Raman Spectroscopy. 2019, 91 (8), 5316–5322. https://doi.org/10.1021/acs.analchem.9b00200.

14) Fang, Y.; Seong, N.-H. .; Dlott, D. D. Measurement of the Distribution of Site Enhancements in Surface-Enhanced Raman Scattering. Science 2008, 321 (5887), 388–392. https://doi.org/10.1126/science.1159499.

15) Chen, S.; Meng, L.; Shan, H.; Li, J.; Qian, L.; Williams, C.; Yang, Z.; Tian, Z.-Q. How to Light Special Hot Spots in Multiparticle–Film Configurations. 2016, 10 (1), 581–587. https://doi.org/10.1021/acsnano.5b05605.

16) Irfan, I.; Qu, J.; Bosi, M.; Luca Seravalli; Yeshchenko, O. A.; Xue, B.; Dong, D.; Lin, Y.; Ran Feng Qiu; Li, B.; Qu, J. Enhancement of Raman Scattering and Exciton/Trion Photoluminescence of Monolayer and Few-Layer MoS2 by Ag Nanoprisms and Nanoparticles: Shape and Size Effects. 2021, 125 (7), 4119–4132. https://doi.org/10.1021/acs.jpcc.0c11421.

17) Li, K.; Liu, G.; Zhang, S.; Dai, Y.; Ghafoor, S.; Huang, W.; Zu, Z.; Lu, Y. A Porous Au–Ag Hybrid Nanoparticle Array with Broadband Absorption and High-Density Hotspots for Stable SERS Analysis. Nanoscale 2019, 11 (19), 9587–9592. https://doi.org/10.1039/c9nr01744e.

18) Wang, C.; Liu, B.; Dou, X. Silver Nanotriangles-Loaded Filter Paper for Ultrasensitive SERS Detection Application Benefited by Interspacing of Sharp Edges. Sensors and Actuators B: Chemical 2016, 231, 357–364. https://doi.org/10.1016/j.snb.2016.03.030.

19) Niu, W.; Zhang, W.; Firdoz, S.; Lu, X. Controlled Synthesis of Palladium Concave Nanocubes with Sub-10-Nanometer Edges and Corners for Tunable Plasmonic Property. Chemistry of Materials 2014, 26 (6), 2180–2186. https://doi.org/10.1021/cm500210u.

20) Bai, Q.; Liang, M.; Wu, W.-L.; Zhang, C.; Li, X.; Liu, M.; Yang, D.; Zhang, Y.; Hu, Q.; Wang, L.; Du, F.; Sui, N.; Zhu, Z. Plasmonic Nanozyme of Graphdiyne Nanowalls Wrapped Hollow Copper Sulfide Nanocubes for Rapid Bacteria-Killing. 2022, 32 (20), 2112683–2112683. https://doi.org/10.1002/adfm.202112683.

21) Cobley, C. M.; Skrabalak, S. E.; Campbell, D. J.; Xia, Y. Shape-Controlled Synthesis of Silver Nanoparticles for Plasmonic and Sensing Applications. Plasmonics 2009, 4 (2), 171–179. https://doi.org/10.1007/s11468-009-9088-0.

22) J. Park; Lee, Y.; Nam, J.-M. Precisely Shaped, Uniformly Formed Gold Nanocubes with Ultrahigh Reproducibility in Single-Particle Scattering and Surface-Enhanced Raman Scattering. 2018, 18 (10), 6475–6482. https://doi.org/10.1021/acs.nanolett.8b02973

23) Yang, X.; He, Q.; Guo, F.; Liu, X.; Chen, Y. Translocation and Biotoxicity of Metal (Oxide) Nanoparticles in the Wetland-Plant System. Frontiers of Environmental Science & Engineering 2021, 15 (6). https://doi.org/10.1007/s11783-021-1432-4.

24) Clément Levard; Hotze, E. M.; Colman, B. P.; Dale, A.; Truong, L.; Yang, X.-Q.; Bone, A. J.; Brown, G. E.; Tanguay, R. L.; Di, R. T.; Bernhardt, E. S.; Meyer, J. N.; Wiesner, M. R.; Lowry, G. V. Sulfidation of Silver Nanoparticles: Natural Antidote to Their Toxicity. Environmental Science & Technology 2013, 47 (23), 13440–13448. https://doi.org/10.1021/es403527n.

25) Roy, N.; Gaur, A.; Jain, A.; Bhattacharya, S.; Rani, V. Green Synthesis of Silver Nanoparticles: An Approach to Overcome Toxicity. Environmental Toxicology and Pharmacology 2013, 36 (3), 807–812. https://doi.org/10.1016/j.etap.2013.07.005.

26) Grade, S.; Eberhard, J.; Jakobi, J.; Winkel, A.; Stiesch, M.; Barcikowski, S. Alloying Colloidal Silver Nanoparticles with Gold Disproportionally Controls Antibacterial and Toxic Effects. Gold Bulletin 2013, 47 (1-2), 83–93. https://doi.org/10.1007/s13404-013-0125-6.

27) Abdel-Aziz El Mel; Stephant, N.; Molina-Luna, L.; Gautron, E.; Haik, Y.; Tabet, N.; Tessier, P.-Y.; Gautier, R. Kirkendall Effect vs Corrosion of Silver Nanocrystals by Atomic

Oxygen: From Solid Metal Silver to Nanoporous Silver Oxide. 2017, 121 (35), 19497–19504. https://doi.org/10.1021/acs.jpcc.7b06030

28) Skrabalak, S. E.; Chen, J.; Sun, Y.; Lu, X.; Au, L.; Cobley, C. M.; Xia, Y. Gold Nanocages: Synthesis, Properties, and Applications. ChemInform 2009, 40 (14). https://doi.org/10.1002/chin.200914224.

29) Ma, Y.; Li, W.; Cho, E. C.; Li, Z.; Yu, T.; Zeng, J.; Xie, Z.; Xia, Y. Au@Ag Core−Shell Nanocubes with Finely Tuned and Well-Controlled Sizes, Shell Thicknesses, and Optical Properties. ACS Nano 2010, 4 (11), 6725–6734. https://doi.org/10.1021/nn102237c.

30) SAME AS 29

31) Yang, M.; Gilroy, K. D.; Xia, Y. A General Approach to the Synthesis of M@Au/Ag (M = Au, Pd, and Pt) Nanorattles with Ultrathin Shells Less than 2.5 Nm Thick. 2017, 34 (8), 1600279–1600279. https://doi.org/10.1002/ppsc.201600279.

32) Mayer, M.; Anja Maria Steiner; Falk Röder; Pötschke, P.; Tobias; Fery, A. Aqueous Gold Overgrowth of Silver Nanoparticles: Merging the Plasmonic Properties of Silver with the Functionality of Gold. 2017, 56 (50), 15866–15870. https://doi.org/10.1002/anie.201708398.

33) M. Luisa Marin; McGilvray, K. L.; Scaiano, J. C. Photochemical Strategies for the Synthesis of Gold Nanoparticles from Au(III) and Au(I) Using Photoinduced Free Radical Generation. Journal of the American Chemical Society 2008, 130 (49), 16572–16584. https://doi.org/10.1021/ja803490n.

34) Au, L.; Lu, X.; Xia, Y. A Comparative Study of Galvanic Replacement Reactions Involving Ag Nanocubes and AuCl2−or AuCl4−. Advanced Materials 2008, 20 (13), 2517–2522. https://doi.org/10.1002/adma.200800255.

35) Sneed, B. T.; Chun Wei Kuo; Brodsky, C. N.; Tsung, C.-K. Iodide-Mediated Control of Rhodium Epitaxial Growth on Well-Defined Noble Metal Nanocrystals: Synthesis, Characterization, and Structure-Dependent Catalytic Properties. 2012, 134 (44), 18417–18426. https://doi.org/10.1021/ja308030h.

36) Skrabalak, S. E.; Au, L.; Li, X.; Xia, Y. Facile Synthesis of Ag Nanocubes and Au Nanocages. Nature Protocols 2007, 2 (9), 2182–2190. https://doi.org/10.1038/nprot.2007.326

37) Smith, J. E.; Griffin, D. K.; Leny, J. K.; Hagen, J. A.; Chávez, J. L.; Kelley-Loughnane, N. Colorimetric Detection with Aptamer-Gold Nanoparticle Conjugates Coupled to an Android-Based Color Analysis Application for Use in the Field. Talanta 2014, 121, 247–255. https://doi.org/10.1016/j.talanta.2013.12.062.

38) Yang, M.; Gilroy, K. D.; Xia, Y. A General Approach to the Synthesis of M@Au/Ag (M = Au, Pd, and Pt) Nanorattles with Ultrathin Shells Less than 2.5 Nm Thick. 2017, 34 (8), 1600279–1600279. https://doi.org/10.1002/ppsc.201600279.

39) Khlebtsov, N.; Dykman, L. A.; Khlebtsov, B.N. Synthesis and Plasmonic Tuning of Gold and Gold-Silver Nanoparticles. 2022, 91. https://doi.org/10.57634/RCR5058.

40) Murphy, C. J.; Sau, T. K.; Gole, A. M.; Orendorff, C. J.; Gao, J.; Gou, L.; Hunyadi, S. E.; Li, T. Anisotropic Metal Nanoparticles: Synthesis, Assembly, and Optical Applications. The Journal of Physical Chemistry B 2005, 109 (29), 13857–13870. https://doi.org/10.1021/jp0516846.

41) Samal, A. K.; Polavarapu, L.; Rodal-Cedeira, S.; Liz-Marzán, L. M.; Pérez-Juste, J.; Pastoriza-Santos, I. Size Tunable Au@Ag Core–Shell Nanoparticles: Synthesis and Surface-Enhanced Raman Scattering Properties. Langmuir 2013, 29 (48), 15076–15082. https://doi.org/10.1021/la403707j.

42) Gong, J.; Zhou, F.; Li, Z.; Tang, Z. Synthesis of Au@Ag Core–Shell Nanocubes Containing Varying Shaped Cores and Their Localized Surface Plasmon Resonances. Langmuir 2012, 28 (24), 8959–8964. https://doi.org/10.1021/la204684u.

43) Singha, D.; Barman, N.; Sahu, K. A Facile Synthesis of High Optical Quality Silver Nanoparticles by Ascorbic Acid Reduction in Reverse Micelles at Room Temperature. Journal of Colloid and Interface Science 2014, 413, 37–42. https://doi.org/10.1016/j.jcis.2013.09.009.

44) Zhang, J.-Y.; Doll, B. A.; Beckman, E. J.; Hollinger, J. O. Three-Dimensional Biocompatible Ascorbic Acid-Containing Scaffold for Bone Tissue Engineering. Tissue Engineering 2003, 9 (6), 1143–1157. https://doi.org/10.1089/10763270360728053.

45) Khan, Z.; Singh, T.; Hussain, J. I.; Hashmi, A. A. Au(III)–CTAB Reduction by Ascorbic Acid: Preparation and Characterization of Gold Nanoparticles. Colloids and Surfaces B: Biointerfaces 2013, 104, 11–17. https://doi.org/10.1016/j.colsurfb.2012.11.017.

46) Chee, S. W.; Tan, S. F.; Baraissov, Z.; Bosman, M.; Mirsaidov, U. Direct Observation of the Nanoscale Kirkendall Effect during Galvanic Replacement Reactions. Nature Communications 2017, 8 (1). https://doi.org/10.1038/s41467-017-01175-2.

47) Mutavdžić, D.; Xu, J.; Thakur, G.; Triulzi, R.; Kasas, S.; Jeremić, M.; Leblanc, R.; Radotić, K. Determination of the Size of Quantum Dots by Fluorescence Spectroscopy. The Analyst 2011, 136 (11), 2391. https://doi.org/10.1039/c0an00802h

48) Liu, J.; He, H.; Xiao, D.; Yin, S.; Ji, W.; Jiang, S.; Luo, D.; Wang, B.; Liu, Y. Recent Advances of Plasmonic Nanoparticles and Their Applications. Materials 2018, 11 (10), 1833. https://doi.org/10.3390/ma11101833.

49) Ma, X.; He, S.; Qiu, B.; Luo, F.; Guo, L.; Lin, Z. Noble Metal Nanoparticle-Based Multicolor Immunoassays: An Approach toward Visual Quantification of the Analytes with the Naked Eye. 2019, 4 (4), 782–791. https://doi.org/10.1021/acssensors.9b00438.

50) Sagle, L. B.; Ruvuna, L. K.; Ruemmele, J. A.; Van Duyne, R. P. Advances in Localized Surface Plasmon Resonance Spectroscopy Biosensing. Nanomedicine 2011, 6 (8), 1447–1462. https://doi.org/10.2217/nnm.11.117.

51) Lee, W.-R.; Eun Kyung Kim; Joon Young Choi; Park, J.-I.; Seung Hwan Ko; Sang Cheul Oh; Cheon, J. Redox−Transmetalation Process as a Generalized Synthetic Strategy for Core−Shell Magnetic Nanoparticles. 2005, 127 (46), 16090–16097. https://doi.org/10.1021/ja053659j.

52) Liu, B.; Wang, Q.; Yu, S.; Zhao, T.; Han, J.; Jing, P.; Hu, W.; Liu, L.; Zhang, J.; Sun, L.-D.; Yan, C.-H. Double Shelled Hollow Nanospheres with Dual Noble Metal Nanoparticle Encapsulation for Enhanced Catalytic Application. Nanoscale 2013, 5 (20), 9747. https://doi.org/10.1039/c3nr02759g.

53) de Villiers, M. M.; Otto, D. P.; Strydom, S. J.; Lvov, Y. M. Introduction to Nanocoatings Produced by Layer-By-Layer (LbL) Self-Assembly. Advanced Drug Delivery Reviews 2011, 63 (9), 701–715. https://doi.org/10.1016/j.addr.2011.05.011.

54) Same as 53

55) Pareek, V.; Bhargava, A.; Gupta, R.; Jain, N.; Panwar, J. Synthesis and Applications of Noble Metal Nanoparticles: A Review. Advanced Science, Engineering and Medicine 2017, 9 (7), 527–544. https://doi.org/10.1166/asem.2017.2027.

56) Yadav, V.; Jeong, S.; Ye, X.; Li, C. W. Surface-Limited Galvanic Replacement Reactions of Pd, Pt, and Au onto Ag Core Nanoparticles through Redox Potential Tuning. Chemistry of Materials 2022, 34 (4), 1897–1904. https://doi.org/10.1021/acs.chemmater.1c04176

57) Zumdahl, S. S.; DeCoste, D. J. Introductory Chemistry; Cengage Learning, 2018.

58) Anderson, B. D.; Tracy, J. B. Nanoparticle Conversion Chemistry: Kirkendall Effect, Galvanic Exchange, and Anion Exchange. Nanoscale 2014, 6 (21), 12195–12216. https://doi.org/10.1039/c4nr02025a

59) Seung Wook Kim; Chung, H.; Jong Hwa Kwon; Ho Il Yoon; Kim, W. Facile Synthesis of Silver Chloride Nanocubes and Their Derivatives. 2010, 31 (10), 2918–2922. https://doi.org/10.5012/bkcs.2010.31.10.2918.

60) Siekkinen, A. R.; McLellan, J. M.; Chen, J.; Xia, Y. Rapid Synthesis of Small Silver Nanocubes by Mediating Polyol Reduction with a Trace Amount of Sodium Sulfide or Sodium Hydrosulfide. Chemical Physics Letters 2006, 432 (4-6), 491–496. https://doi.org/10.1016/j.cplett.2006.10.095.

61) Luo, C.; Zhang, Y.; Zeng, X.; Zeng, Y.; Wang, Y. The Role of Poly(Ethylene Glycol) in the Formation of Silver Nanoparticles. Journal of Colloid and Interface Science 2005, 288 (2), 444–448. https://doi.org/10.1016/j.jcis.2005.03.005.

62) Das, R.; Sarkar, S. Optical Properties of Silver Nano-Cubes. Optical Materials 2015, 48, 203–208. https://doi.org/10.1016/j.optmat.2015.07.038

63) Sun, Y.; Xia, Y. Shape-Controlled Synthesis of Gold and Silver Nanoparticles. ChemInform 2003, 34 (10). https://doi.org/10.1002/chin.200310226.

64) Ahmad, N.; Bon, M.; Passerone, D.; Erni, R. Template-Assisted in Situ Synthesis of Ag@Au Bimetallic Nanostructures Employing Liquid-Phase Transmission Electron Microscopy. 2019, 13 (11), 13333–13342. https://doi.org/10.1021/acsnano.9b06614